Space Weather

RESEARCH ARTICLE
10.1029/2023SW003767

Key Points:

- Typical substorm-time ground *dB*/*dt* variations (5–10 nT/s) are caused by interplanetary shocks with moderate inclinations (140°–160°)
- The more frontal the shock, the more intense and the broader the ionospheric current amplitudes
- The more frontal the shock, the more intense, larger the area coverage, and the lower the equatorward latitudinal extent of *dB*/*dt* variations

Supporting Information:

Supporting Information may be found in the online version of this article.

Correspondence to:

D. M. Oliveira,
denny@umbc.edu

Citation:

Oliveira, D. M., Weygand, J. M., Coxon, J. C., & Zesta, E. (2024). Substorm-time ground *dB*/*dt* variations controlled by interplanetary shock impact angles: A statistical study. *Space Weather*, *22*, e2023SW003767. https://doi.org/10.1029/2023SW003767

Received 23 OCT 2023
Accepted 16 FEB 2024

Author Contribution:

Conceptualization: Denny M. Oliveira
Methodology: Denny M. Oliveira
Software: Denny M. Oliveira

Substorm-Time Ground *dB*/*dt* Variations Controlled by Interplanetary Shock Impact Angles: A Statistical Study

Denny M. Oliveira[1,2], James M. Weygand[3], John C. Coxon[4], and Eftyhia Zesta[2]

[1]Goddard Planetary Heliophysics Institute, University of Maryland, Baltimore, MD, USA, [2]Geospace Physics Laboratory, NASA Goddard Space Flight Center, Greenbelt, MD, USA, [3]Department of Earth, Planetary, and Space Sciences, University of California Los Angeles, Los Angeles, CA, USA, [4]Department of Mathematics, Physics and Electrical Engineering, Newcastle Upon Tyne, UK

Abstract In this study, we investigate the effects caused by interplanetary (IP) shock impact angles on the subsequent ground *dB*/*dt* variations during substorms. IP shock impact angles have been revealed as a major factor controlling the subsequent geomagnetic activity, meaning that shocks with small inclinations with the Sun-Earth line are more likely to trigger higher geomagnetic activity resulting from nearly symmetric magnetospheric compressions. Such field variations are linked to the generation of geomagnetically induced currents (GICs), which couple to artificial conductors on the ground leading to deleterious consequences. We use a sub-set of a shock data base with 237 events observed in the solar wind at L1 upstream of the Earth, and large arrays of ground magnetometers at stations located in North America and Greenland. The spherical elementary current system methodology is applied to the geomagnetic field data, and field-aligned-like currents in the ionosphere are derived. Then, such currents are inverted back to the ground and *dB*/*dt* variations are computed. Geographic maps are built with these field variations as a function of shock impact angles. The main findings of this investigation are: (a) typical *dB*/*dt* variations (5–10 nT/s) are caused by shocks with moderate inclinations; (b) the more frontal the shock impact, the more intense and the more spatially defined the ionospheric current amplitudes; and (c) nearly frontal shocks trigger more intense *dB*/*dt* variations with larger equatorward latitudinal expansions. Therefore, the findings of this work provide new insights for GIC forecasting focusing on nearly frontal shock impacts on the magnetosphere.

Plain Language Summary Space weather effects caused by solar perturbations can increase the intensity of electric currents flowing in the Earth's upper atmosphere. These currents in turn induce geoelectric currents on the ground that couple with ground infrastructure, such as power transmission lines, oil/gas pipelines, and railways, which further cause deleterious consequences. Recent studies have shown that the angle with which solar perturbations impact the Earth closely controls intensifications of electric currents in the upper atmosphere and the subsequent ground magnetic field perturbations causing geoelectric currents. When these space weather drivers impact Earth more frontally, the resulting atmospheric current enhancements and the subsequent ground magnetic field perturbations are generally more intense. In this study, we use a large amount of magnetic field data recorded in North America and Greenland. We find that the most intense geomagnetic field disturbances are caused by the impacts of nearly frontal solar perturbations on the Earth and cover large geographic areas reaching southern Canada and northern United States. The results of this work can be used by space weather forecasters when predicting events with significant magnetic field variations leading to intense geoelectric currents, particularly when tracking space weather drivers that are forecasted to impact Earth nearly frontally.

1. Introduction

The Sun is a magnetically active star that generates the constant expansion of a ubiquitous plasma, named the solar wind, that flows away in the heliosphere. Solar disturbances are created on the Sun's surface and propagate explosively away and can be observed in many heliospheric regions (Echer, 2019; Hajra, 2021; Harada et al., 2017; Lamy, 2020; Mostafavi et al., 2022; Pérez-Alanis et al., 2023; Winslow et al., 2015). If the disturbance speed with respect to the ambient solar wind flow speed is greater than the local magnetosonic speed, a fast forward interplanetary (IP) shock is formed (Burlaga, 1971; Schwartz, 1998; Stone & Tsurutani, 1985). The strengths of IP shocks are frequently determined by means of solar wind parameters such as the ratio of downstream to upstream plasma densities and shock Mach numbers (Andréeová & Přech, 2007; Lugaz et al., 2016; Tsurutani & Lin, 1985). When IP shocks strike the Earth's magnetosphere, many geomagnetic perturbations are observed in the magnetosphere-ionosphere (MI) system, including magnetic field perturbations in geosynchronous orbit (Villante & Piersanti, 2011; C. Wang et al., 2010), ultra-low frequency wave activity (C.-R. Wang et al., 2010; Zong et al., 2009), satellite orbital drag (Krauss et al., 2018; Oliveira & Zesta, 2019), ionospheric disturbances (Belakhovsky et al., 2017; Liu et al., 2023), and sudden impulse signatures observed by ground magnetometers around the world (Chao & Lepping, 1974; Russell et al., 1994; Smith et al., 2020). Therefore, understanding IP shock geoeffectiveness is of paramount importance in space weather investigations (Alves et al., 2011; Echer et al., 2004; Su et al., 2009).

In addition to solar wind parameters, the shock impact angle, the angle the shock normal vector performs with the Sun-Earth line, has been shown to be a major factor controlling shock geoeffectiveness. For example, in general, numerical simulations and data analyses show that the more frontal the shock, the shorter the rise times of positive sudden impulses recorded by ground magnetometers worldwide (Rudd et al., 2019; Takeuchi et al., 2002; C. Wang et al., 2006). Additionally, nearly frontal shocks are more likely to trigger ultra-low frequency waves with intense wave power (Oliveira & Raeder, 2014; Oliveira et al., 2020; Rubtsov et al., 2023; Takahashi et al., 2023), and more intense field-aligned currents in the MI system (Guo et al., 2005; Selvakumaran et al., 2017; Shi et al., 2019). Oliveira and Samsonov (2018) and Oliveira (2023a) have reviewed the topic of geomagnetic activity triggered by shocks with different orientations.

Impacts of IP shocks on the magnetosphere can enhance two major Earth's current systems: (a) the magnetopause current in the magnetosphere (>10 Earth radii), and (b) the auroral electrojet currents in the ionosphere (∼120 km altitude) (Cowley, 2000; Fiori et al., 2014; Milan et al., 2017). Magnetospheric substorms occur when large amounts of electromagnetic energy are explosively released from the Earth's magnetotail and mapped down into the ionosphere (Akasofu, 1981; Burch, 1972; Kalmoni et al., 2018; Sitnov et al., 2019). Such substorm activity enhances the auroral electrojets (Gjerloev et al., 2004; Kamide & Nakamura, 1996) leading to intense magnetic field variations (dB/dt) on the ground (Freeman et al., 2019; Ngwira et al., 2018; Piccinelli & Krausmann, 2018; Viljanen et al., 2006). According to Faraday's law curl $\mathbf{E} = -d\mathbf{B}/dt$, such field variations couple with artificial conductors on the ground leading to the generation of geomagnetically induced currents (GICs) flowing in the conductors, which are detrimental to power infrastructure, oil/gas pipelines, and railway infrastructure (Molinski, 2002; Oliveira & Ngwira, 2017; Patterson et al., 2023; Piersanti & Carter, 2020; Pulkkinen et al., 2013; Smith et al., 2022; Thaduri et al., 2020; Tsurutani & Hajra, 2021).

Shock impact angle effects on the subsequent substorm triggering was first investigated by Oliveira and Raeder (2014) with numerical simulations. The authors simulated the impacts of two shocks on the magnetosphere, with one being a moderate frontal impact, and the other, a strong inclined impact. Oliveira and Raeder (2014) noted that intense substorm activity occurred after the frontal shock impact, whereas the substorm activity following the inclined shock impact was mild, even though the inclined shock was stronger than the frontal shock. Following that work, Oliveira and Raeder (2015) performed a statistical analysis with hundreds of shock events and a global array of ground magnetometers to study the shock impact angle effects on the subsequent substorm activity. The authors concluded that the faster and the more frontal the shock, the more intense the westward auroral electrojet, a well-known substorm signature (Davis & Sugiura, 1966; Gjerloev et al., 2004; Kamide & Nakamura, 1996). More recently, Oliveira et al. (2021) performed a comparative study of two similarly strong shocks, with one being nearly frontal, and the other, highly inclined, to investigate the subsequent dB/dt variations during the respective substorm activity. The authors used ground magnetometer data from stations in North America and Greenland. Oliveira et al. (2021) concluded that dB/dt variations occurred faster, were stronger, and covered larger geographic areas in the frontal case when compared to the inclined case. The general conclusion of the works mentioned above is that nearly frontal impacts compress the magnetosphere almost symmetrically setting the stage with favorable conditions for effective energy release by the magnetotail, which does not clearly occur with inclined shock impacts (Oliveira, 2023a; Oliveira & Samsonov, 2018).

The goal of this work is to follow up on the case study published by Oliveira et al. (2021) and perform a superposed epoch analysis and statistical study of shock impact angle effects on ground dB/dt variations during the subsequent substorms triggered by the shocks. Section 2 describes the data and methodology used in this study. Results are shown in Section 3, and a discussion of the results is presented in Section 4. Finally, Section 5 summarizes and concludes the paper.

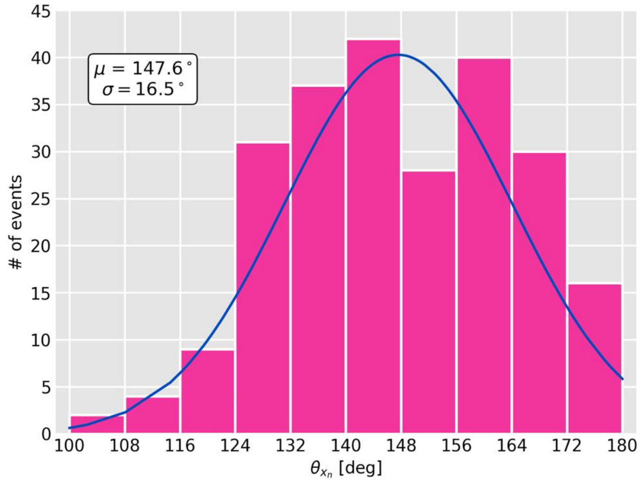

Figure 1. Magenta bars: Number distribution of shock impact angles for the 237 events here investigated. Thick blue line: Gaussian curve fitted to the shock impact angle number distribution. The values shown in the plot are the mean (μ) and standard deviation (σ).

2. Data and Methodology

2.1. Interplanetary Shock Data Base

The fast forward IP shock data base published by Oliveira (2023b) is used in this study. Solar wind plasma and interplanetary magnetic field (IMF) data measured by Wind and Advanced Composition Explorer spacecraft were used to compile the list. The original list has 603 events from January 1995 to May 2023.

The IP shock impact angle, θ_{x_n}, is defined as the angle the shock normal vector performs with the Sun-Earth line. Basically, equations using magnetic field data and solar wind velocity data (and combinations of both data sets) are used to compute shock impact angles (Abraham-Shrauner, 1972; Cole, 1962; Oliveira, 2017; Oliveira & Samsonov, 2018; Schwartz, 1998). If data of a single satellite is available, a tri-dimensional normal vector $\mathbf{n} = (n_x, n_y, n_z)$ can be obtained, from which the shock impact angle

$$\theta_{x_n} = \cos^{-1}(n_x) \tag{1}$$

can be computed. Since this angle is written in GSE (geocentric solar ecliptic) coordinates, an angle of 180° indicates a purely head-on (frontal) shock. As a result, the shock becomes more inclined as θ_{x_n} decreases. Assumptions of energy and momentum conservation, represented by the Rankine-Hugoniot jump conditions (Jeffrey & Taniuti, 1964; Oliveira, 2017; Priest, 1981), are used in the calculations of shock-related parameters including the shock normal vector **n**. Figure 1 of Oliveira (2023a) brings schematic representations of a purely frontal shock and a highly inclined shock.

Figure 1 shows the shock impact angle number distribution for the 237 shock events here investigated (magenta bars). Only a sub-set of the events provided by Oliveira (2023b) is used in this study due to availability limitations imposed by one of the main data sets here used (see Section 2.3). The thick blue line is a Gaussian curve fitted to the histogram. For this sub-data set, the mean θ_{x_n} value is $\mu = 147.6°$, and the standard deviation is $\sigma = 16.5°$. Therefore, a typical shock event in the data base has a moderate inclination (see equations below).

According to the θ_{x_n} definition, shock impact angles can be classified as follows:

$$\theta_{x_n} < 140° \qquad \text{Highly inclined shocks} \tag{2}$$

$$140° \leq \theta_{x_n} < 160° \qquad \text{Moderately inclined shocks} \tag{3}$$

$$\theta_{x_n} \geq 160° \qquad \text{Nearly frontal shocks} \tag{4}$$

Figure 2 shows a histogram for the number distributions, with respect to shock inclination category, of the 237 events used in this study. The blue bar indicates all shocks (ALL); green bar, highly inclined shocks (HIS); orange bar, moderately inclined shocks (MIS); and red bar, nearly frontal shocks (NFS). The relative distributions of these three shock inclination categories are shown in the pie diagram inset in the figure. The relative number distributions of these categories vary from ~30%–35%, with more shocks in the MIS class, fewer shocks in the NFS class, and HIS class in between. Although less frequent, NFS tend to occur more often during times of high solar activity as represented by sunspot numbers: in general, the higher the yearly sunspot numbers, the higher the annual number distribution of IP shocks, including NFS (Kilpua et al., 2015; Oliveira, 2023b; Rudd et al., 2019).

2.2. Ground Magnetometer Data

We use ground magnetometer data recorded by stations located in North America (from Alaska to Labrador/Colorado to Nunavut) and Greenland (west coast) to compute ionospheric current amplitudes and corresponding *dB*/*dt* variations on the ground. The main ground magnetometer data is provided by the Time History of Events and Macroscale Interactions during Substorms (THEMIS) ground magnetometer (GMAG) array, with resolution of 1–2 Hz (Mende et al., 2008; Russell et al., 2008). In addition to THEMIS/GMAG, other ground magnetometer

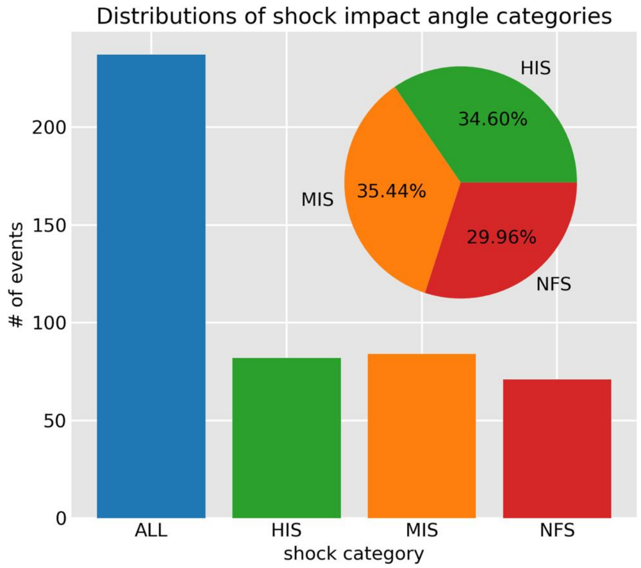

Figure 2. Colored bars: Shock number distributions of the 237 events in the shock data base broken into the shock impact angle categories shown in Equations 2–4. Inset pie diagram: Relative percentile of the number of shocks within each angle category.

arrays are used to complement calculations. The THEMIS/GMAG and additional ground magnetometers are referred to as SECS stations in this paper. More details about the additional arrays, including their stations' names and geographic locations, are provided in Supporting Information S1.

2.3. The Spherical Elementary Current System (SECS) Technique

The Spherical Elementary Current System (SECS) method (Amm & Viljanen, 1999) is applied to the ground magnetometer data described above to obtain a bi-dimensional picture of the ionospheric currents. As described by Weygand et al. (2011), ionospheric current amplitudes are computed at 100 km altitude with SECS by means of inverted magnetic field fluctuations decomposed to single values. This procedure yields two outputs, one being the equivalent ionospheric currents, and the other, the real Hall and Pedersen currents (Weygand et al., 2012). First, ionospheric equivalent currents, the divergence-free currents that are horizontal to the ground, are computed. Second, equivalent ionospheric currents are used to derive the current amplitudes, which are the curl-free currents that are perpendicular to the ionosphere (not field aligned currents, but a proxy for the field-aligned current) (Amm et al., 2002) The spatial resolutions of the equivalent currents is 6.9° in geographic longitude and 2.9° in geographic latitude, whereas the spatial resolutions of the current amplitudes are 1.5° and 3.5° in geographic latitude and longitude, respectively. The time resolution of both SECS currents is 10 s. The only SECS current output used in this work are the SECS ionospheric current amplitudes, henceforth referred to as SECS currents.

The Biot-Savart law (Jackson, 1999) is applied to both SECS currents to obtain the horizontal ground dB/dt variations given by $dB/dt = \sqrt{(dB_x/dt)^2 + (dB_y/dt)^2}$. Here, dB_x/dt and dB_y/dt are the northward and eastward components of the geomagnetic field variations. The Fukushima theorem (Fukushima, 1994) states that, in all regions below the ionosphere, magnetic fields generated from field-aligned currents and their corresponding Pedersen currents cancel each other out. However, this theorem is only valid for the ionosphere with constant conductance, which is not the case during storms and substorms when conductances can vary by a few siemens (Stepanov et al., 2021). More details of the use of the SECS technique to obtain dB/dt variations can be found elsewhere (Weygand, 2021; Weygand et al., 2011, 2012).

Since both SECS data sets (currents and dB/dt variations) used in this study span from January 2007 to December 2022, we use events from the shock list corresponding to the same time range, hence the 237 events shown in the first two figures. We use SECS data as opposed to deriving dB/dt variations directly from in-situ ground magnetometer data because many interpolation techniques fail in areas of the map that are not well populated by magnetometers such as northern Canada or the middle of Hudson Bay.

2.4. Field-Aligned Current Densities From AMPERE

Active Magnetosphere and Planetary Electrodynamics Response Experiment (AMPERE) data are used in this study as a supporting data set. AMPERE is a data set of Birkeland currents that combines magnetic field perturbations from Iridium satellites by spherical harmonic fitting. The data processing techniques have been documented by Anderson et al. (2000) and Waters et al. (2020). The AMPERE current density is found on a grid with resolutions of 1° in magnetic latitude (MLAT) and 1 hr of magnetic local time (MLT), computed at 780 km altitude in Altitude-Adjusted Corrected GeoMagnetic (AACGM) coordinates (Baker & Wing, 1989; Shepherd, 2014) using the International Geomagnetic Reference Field (IGRF) model (Alken et al., 2021). The AMPERE currents used in this study are computed every 2 min in long sliding windows of 10 min. We use AMPERE data from January 2010 to December 2022, so this period corresponds to 201 events in Oliveira (2023b)'s IP shock data base. Birkeland current research using AMPERE data has been reviewed by Coxon et al. (2018).

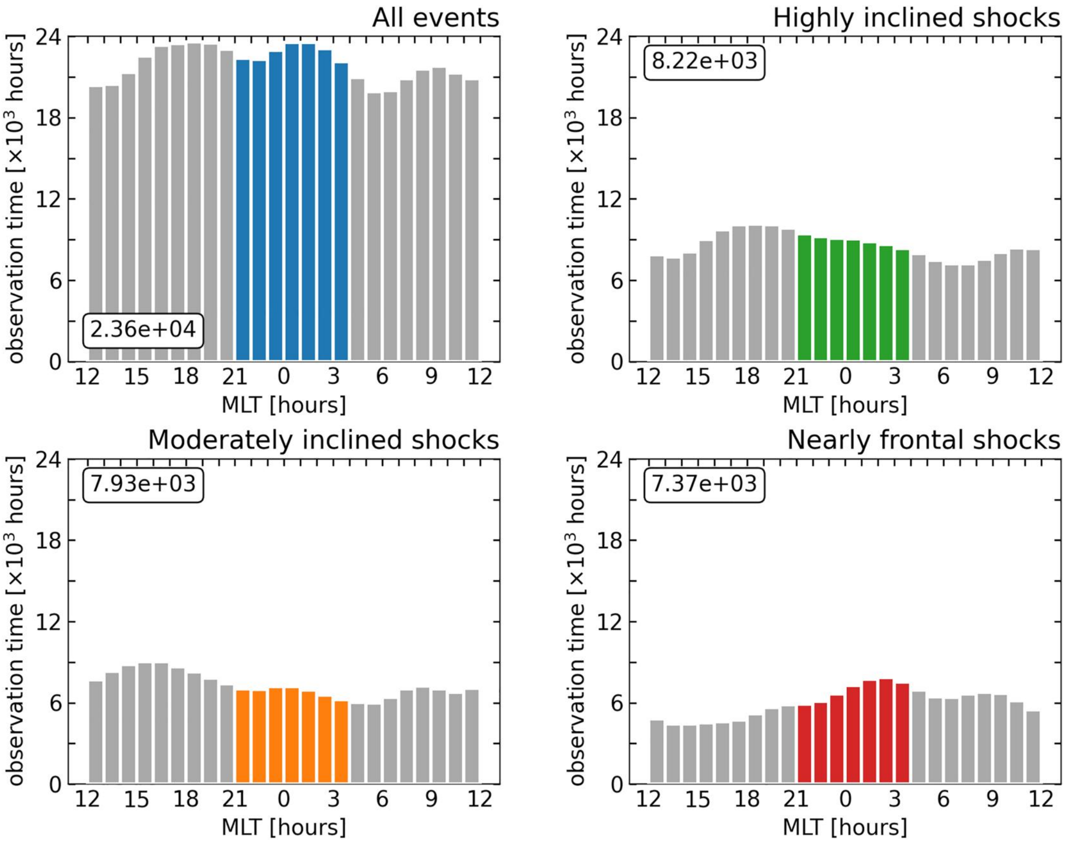

Figure 3. SECS data time distributions (in hours) produced by the SECS stations as a function of MLT (magnetic local time) used in this study (1 SECS data output ≡ 10 s). Colored bars (blue, all events; green, highly inclined shocks; orange, moderately inclined shocks; and red, nearly frontal shocks) correspond to observation times around the magnetic midnight terminator, namely MLT ≤ 03 hr or MLT ≥ 21 hr. Gray bars indicate otherwise. Numbers within boxes represent the average time of SECS data outputs corresponding to the colored bars in each shock category.

3. Results

3.1. Filtering the Data to Account for Substorm Activity

Effects of shock impact angles on the subsequent ground dB/dt variations right after shock impacts were studied by Oliveira et al. (2018). The authors looked at dB/dt variation peaks in a time interval of 10 min after each corresponding shock impact. However, in this study, we look at SECS current and SECS dB/dt variations in a time interval t such that 10 min $< t <$ 180 min after shock impacts as an attempt to exclude effects of shock compressions and capture only substorm-related effects. According to Bargatze et al. (1985), this upper time limit is adequate to account for geomagnetic activity triggered by solar wind drivers including IP shocks, as demonstrated with shock-triggered substorm-like activity by Oliveira and Raeder (2015), and by Freeman and Morley (2004), with a minimal model under constant solar wind driving.

The choice of filtering data is also based on the comparative studies provided by Ngwira et al. (2018) and Oliveira et al. (2021). These works showed that intense ground dB/dt variations after shock impacts occur on the nightside and are highly correlated with energetic particle injections observed by spacecraft on the nightside of the magnetosphere. Such energetic particle injections are usually caused by flux growth phase dropouts attributed to the tailward stretching of the geomagnetic field near MLT = 00 hr (Reeves & Henderson, 2001), which are also supported by substorm auroral image observations (Zhou & Tsurutani, 2001). In Ngwira et al. (2018)'s and Oliveira et al. (2021)'s observations, the ground stations were located in North America and the spacecraft (THEMIS and Los Alamos National Laboratory) were magnetically conjugated with the stations during the corresponding observations, with all stations and satellites locates in intervals within a few hours of the magnetic

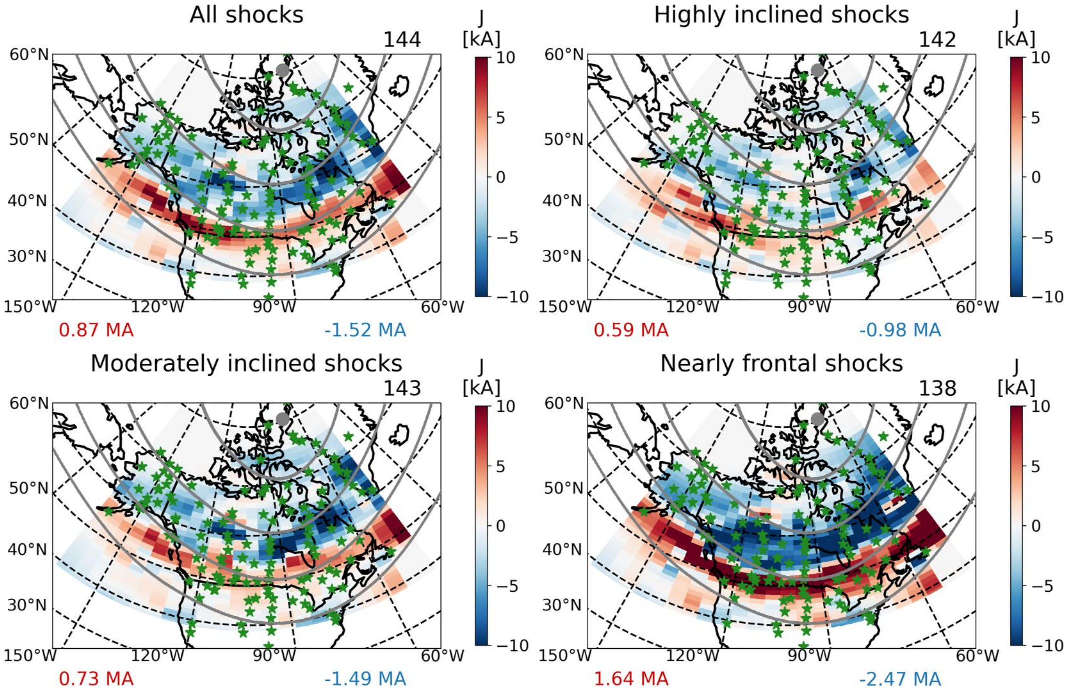

Figure 4. Superposed epoch analysis of SECS current maps of conical projections in North America and Greenland for all shocks (top left), highly inclined shocks (top right), moderately inclined shocks (bottom left), and nearly frontal shocks (bottom right). Blue colors indicate negative downward currents, whereas red colors indicate positive upward currents. The green stars indicate the geographic positions of the SECS stations, and the thick gray lines show AACGM magnetic latitudes from 50° in 10°-increments poleward at 100 km altitude. The numbers on the top right edge of each panel indicate the number of individual SECS stations used to obtain amplitude currents for each shock inclination category. The negative and positive numbers in the bottom edges of each panel indicate the total integrated inward (blue) and outward (red) currents, respectively, in MA, associated with each shock inclination category.

midnight terminator. For this reason, our filtered data are useful to visualize magnetotail activity triggered by shocks when data are plotted in geographic coordinates, as shown in the following sections.

Figure 3 shows SECS data outputs (1 SECS data output ≡ 10 s) as a function of MLT for all events (top left); HIS (top right); MIS (bottom left); and NFS (bottom right). In order to isolate effects of substorms on ground dB/dt variations, SECS data are filtered around the magnetic midnight with either MLT ≤ 03 hr or MLT ≥ 21 hr within the time interval described above and are shown in the colored bars for each shock category. Although there are some marginal variations of observation times in each shock category, there is an average of nearly 7,000–8,000 hr of SECS data outputs considering the substorm MLT hour bins for each shock category. The numbers indicated in each box correspond to the mean time of SECS data output of the MLT outputs represented in the corresponding colored bars for each shock inclination category. Therefore, any eventual MLT biases in the data can be neglected in our analysis.

3.2. Shock Impact Angle Effects on SECS Currents

Figure 4 shows results of superposed epoch analyses of SECS currents for all events (upper left panel); HIS (upper right panel); MIS (lower left panel); and NFS (lower right panel). In this figure, downward Region 1 (R1) currents are indicated by negative current values (blue colors), whereas upward Region 2 (R2) currents are indicated by positive current values (red colors). SECS currents are averaged in 1.5° × 3.5° geographic latitude × longitude bins on a conical projection. The gray lines and the gray circles correspond to AACGM MLATs at 100 km altitude (from 50° northward in increments of 10°) and the geographic position of the magnetic north pole, respectively. Geomagnetic coordinates shown in this paper were computed for 4 June 2015. The green stars in the figure represent the geographic positions of the SECS stations used in this study. The numbers at the top right corner of each panel indicate the numbers of individual stations whose data were used in the corresponding shock category analysis.

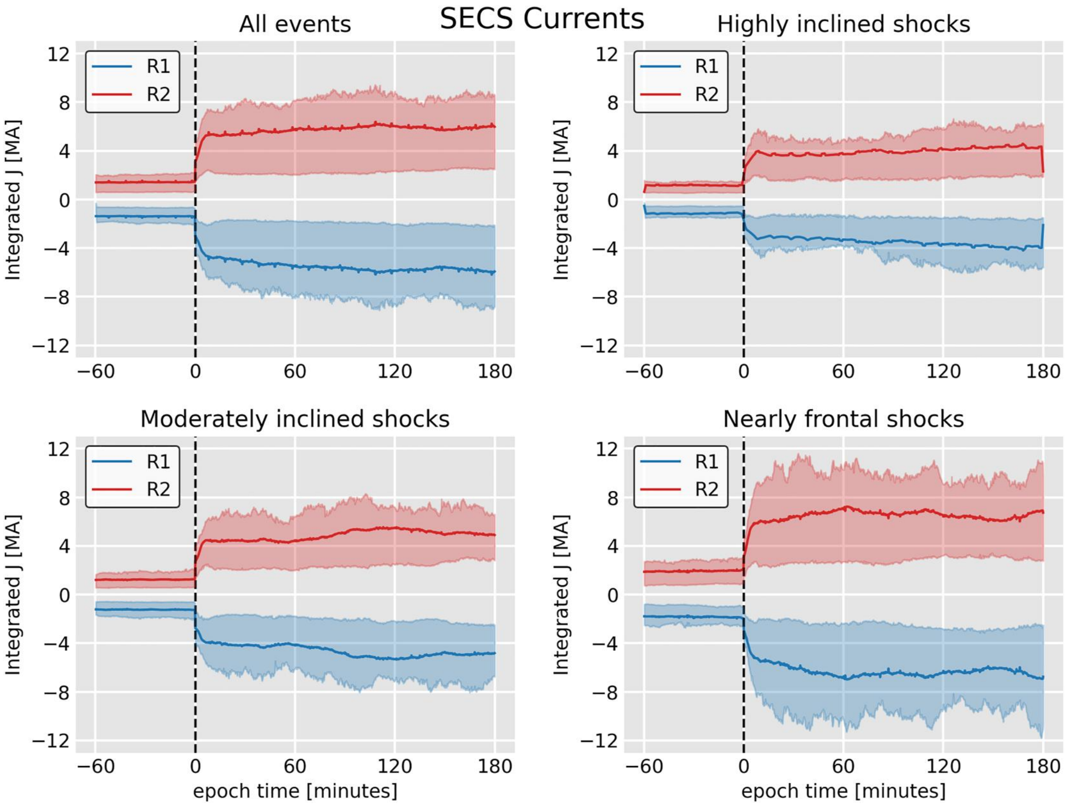

Figure 5. Temporal superposed epoch analysis of the total SECS currents, in MA, moving downwards (Region 1 currents, blue colors), and upwards (Region 2 currents, red color). Mean (thick lines), 20% percentile (lower highlighted limit), and 80% percentile (upper highlighted limit) values are shown in the figure. Top left: all events; top right; highly inclined shocks; bottom left, moderately inclined shocks; and bottom right, nearly frontal shocks.

Results show that the overall downward and upward SECS currents are more intense as the angles in the shock category become more frontal, as shown by values in blue and red at the bottom corners of each panel. This is indicated by the total downward and upward currents integrated in the (10, 180) minute interval after shock impacts and represented in the left and right corners of each panel. Additionally, more spatially defined R1 and R2 current patterns are seen particularly for the NFS category because substorms triggered by NFS are generally more intense due to nearly symmetric magnetospheric compression and more effective magnetotail energy release (Oliveira & Raeder, 2014; Oliveira et al., 2021; Shi et al., 2019).

Temporal superposed epoch analyses of SECS currents for all shock categories are shown in Figure 5. SECS current data are not MLT-filtered in this case (no emphasis on substorm times) and are plotted in a time interval of 1 hr and 3 hr around the shock impact time on the magnetosphere, the zero epoch time, as indicated in the Oliveira (2023b) shock catalog. A 1-min smoothing filter is passed on the data. The shock inclination categories are the same as displayed in the previous figure. In Figure 5, blue colors indicate R1 currents, whereas red colors indicate R2 currents. The highlighted regions indicate the 20% percentile (lower limit) and the 80% percentile (upper limit), while the thick lines indicate mean current values. Percentile and mean values in all panels show two well-known features: (a) SECS currents are more intense, and (b) sudden impulse rise times are shorter as the shock becomes more frontal. Since similar results were published with careful statistical analyses before with AMPERE data by Shi et al. (2019), we do not perform any further statistical analyses of these well-known current features. Moreover, our results indicate a strong influence of shock impact angles on the subsequent SECS current response to shock impacts, confirming the results provided by Shi et al. (2019).

3.3. Shock Impact Angle Effects on Ground *dB*/*dt* Variations

One of the main goals of this research paper is to assess the geographic coverage and equatorward latitudinal extensions of ground *dB*/*dt* variations during substorms triggered under different magnetospheric compression

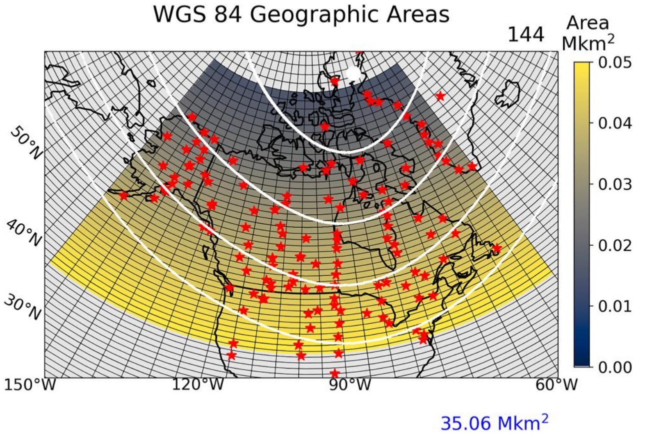

Figure 6. Geographic areas in North America and Greenland, in Mkm^2, with ground SECS stations as a function of geographic latitudes plotted on a conical map projection. The number in blue (35.06 Mkm^2) indicates the total area coverage. The white lines correspond to the magnetic latitudes in AACGM coordinates in 4 June 2015. Geographic and geodetic standards provided by the World Geodetic System (WGS 84) were used in the calculations. The red stars indicate the geographic locations of the SECS stations used in this study.

conditions. For this reason, we show in Figure 6 geographic areas in North America and Greenland with SECS station coverage plotted on a conical projection map. The figure shows geographic areas, in Mkm^2, computed with World Geodetic System standards (Kumar, 2009; Moritz, 2000) that take into consideration the ellipsoid shape of the Earth. The white lines are the magnetic latitudes in AACGM coordinates from 50° to 80°. The grid resolution is $1^\circ \times 5^\circ$ in latitude and longitude, is explicitly shown in the figure. Since the bins are located on a spherical grid, bin areas become slightly larger at lower latitudes (Snyder, 1993). Therefore, this will bring more importance to low-latitude areas with intense ground dB/dt variations as will be shown below in Figures 8–10. The Supporting Information S1 brings detailed information on how the areas shown in Figure 6 are computed.

Figure 7 shows geographic maps of data coverage for SECS data outputs with data filtered around the midnight magnetic local time (MLT $\leq$ 03 hr; MLT $\geq$ 21 hr). The plot shows 1 count $\equiv$ 10-s data points of both SECS data outputs (currents and ground dB/dt variations). The figure is in the same format as in Figure 4. The bin resolution is 1° for latitude, and 5° for longitude. Counts are color coded in the plots. Although there is slightly more coverage eastward of 90°W longitude (HIS) and 60°W longitude (MIS), results show that the total data counts is roughly spread out in the three shock inclination categories (around $\sim 2.25 \times 10^7$ counts, shown in the bottom right corner of each panel) with neglectable variations among the categories. These coverages agree with the MLT distributions shown in Figure 3, since the

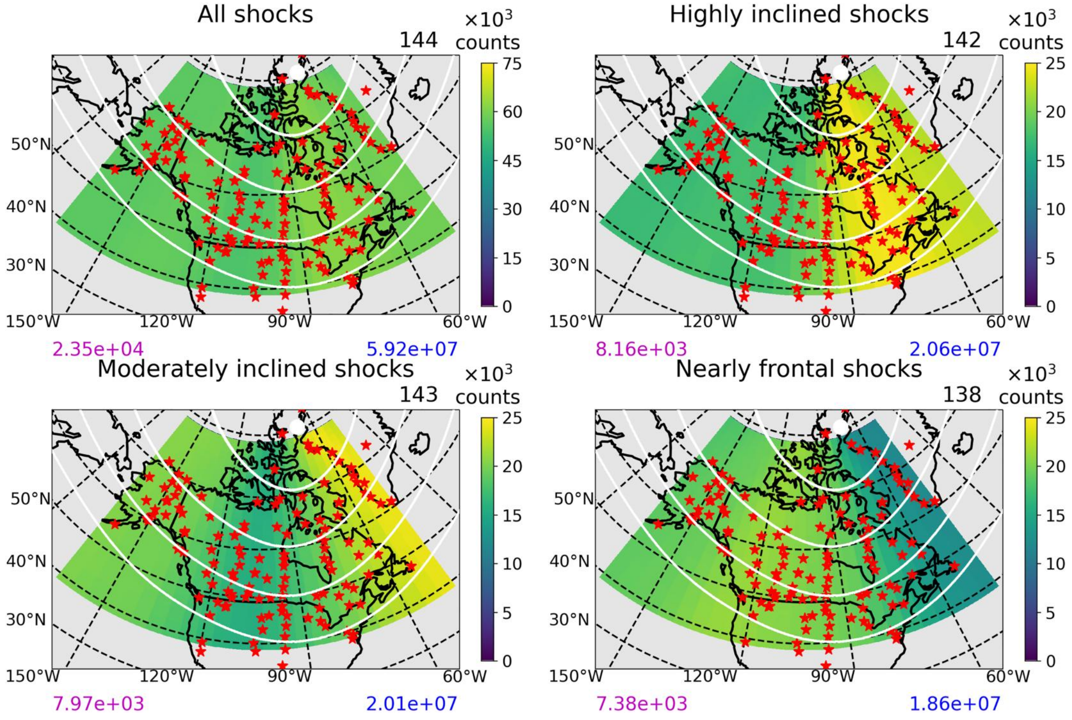

Figure 7. Number of data outputs produced by the SECS technique in the geographic area covering North America and Greenland for all events and the three shock inclination categories. SECS data are filtered with MLT $\leq$ 3 hr or MLT $\geq$ 21 hr. The thick white lines indicate AACGM magnetic latitudes, and the red stars indicate SECS stations. The numbers shown in the right top part of each panel represent the total number of stations used to obtain SECS data within each respective shock inclination category. In the bottom part of each panel, the numbers in blue show the total number of counts, and the numbers in magenta show the average number of hourly SECS data outputs.

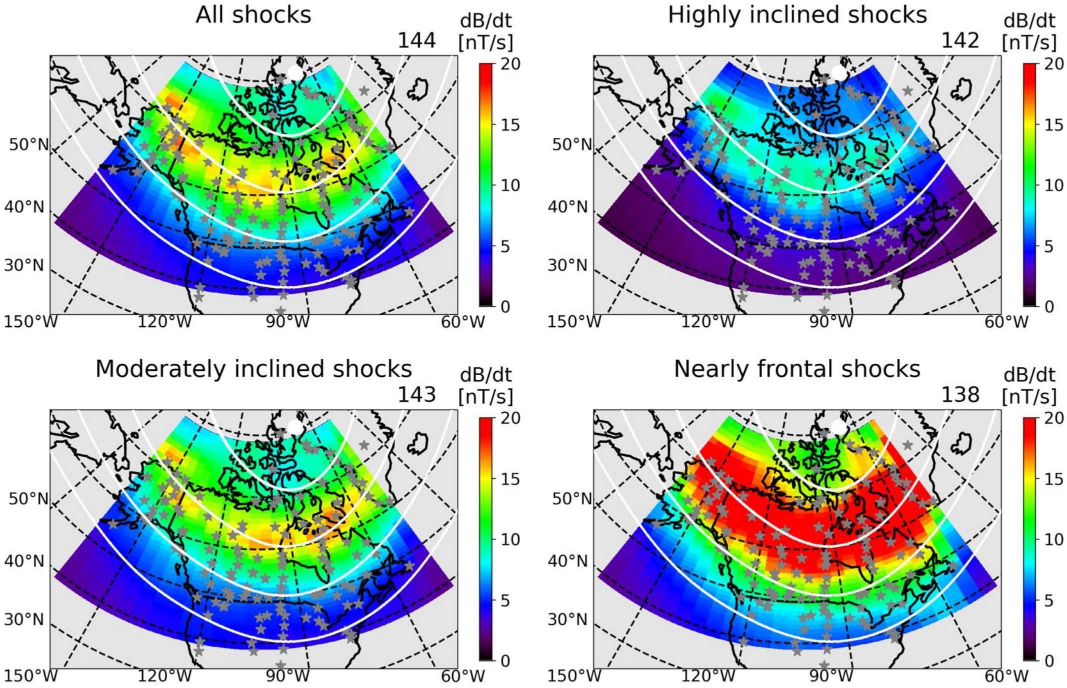

Figure 8. Same as in Figure 7, but for SECS ground d*B*/d*t* variations.

numbers in magenta, representing the average SECS data outputs in hours, are very similar to the average counts (represented in hours, numbers in boxes) shown in Figure 3. Therefore, any eventual significant biases introduced by the number of events in each shock category is practically non-existent.

Geographic maps in North America and Greenland with SECS ground *dB*/*dt* variations are shown in Figure 8. The format and grid resolution of this figure are the same as the ones shown in Figure 7. The data shown in the figure is also filtered around the midnight magnetic terminator. Ground *dB*/*dt* variations in the HIS case show the weakest enhancements. *dB*/*dt* variations lower than 2 nT/s are observed in regions with MLAT $< 60°$. Enhancements of *dB*/*dt* > 5 nT/s are seen in regions above 60° magnetic latitudes. Even higher *dB*/*dt* variations, ∼10 nT/s, are seen in regions with $65° <$ MLAT $< 80°$. Results for all cases and MIS are very similar in terms of intensities and geographic area coverage. In these cases, relatively low-level *dB*/*dt* variations (5 nT/s) are observed below MLAT = 60°, and higher than ∼10 nT/s are observed above this MLAT region. A significant area around MLAT = 70° is seen with *dB*/*dt* variations near 15 nT/s in mid-latitude Canada. More intense *dB*/*dt* variations reach lower latitudes in all events and the category of MIS in comparison to the HIS case. As expected, the case of NFS is the most geoeffective one. Intense *dB*/*dt* variations of ∼10 nT/s reach magnetic latitudes as low as 55°, whereas *dB*/*dt* > 10 nT/s are observed in all magnetic latitudes greater than 60°. More importantly, the NFS case shows a region between ∼65° and ∼80° with very intense field variations with *dB*/*dt* surpassing 20 nT/s. Therefore, the NFS case shows larger areas with the most intense and equatorward latitudinal extensions of *dB*/*dt* variations in all three shock inclination category cases.

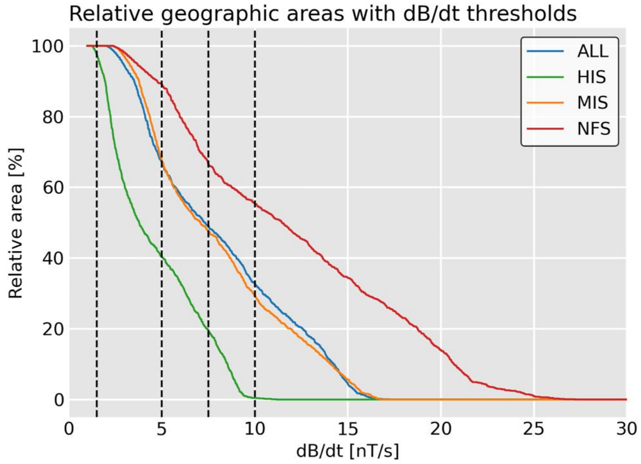

Figure 9. Relative geographic area coverages with specific d*B*/d*t* thresholds for each shock inclination category: Blue, all events (ALL); green, highly inclined shocks (HIS); orange, moderately inclined shocks (MIS); and red, nearly frontal shocks (NFS).

In order to quantify the geographic area coverage of ground *dB*/*dt* variations during the shock-induced substorms, we sum the areas of each geographic bin shown in Figure 6 with *dB*/*dt* variations in the corresponding bin (Figure 8) surpassing a range of specific *dB*/*dt* threshold values. This is shown in Figure 9. In the figure, the blue line indicates results for all shocks; green, HIS; orange, MIS; and red, NFS. The plot shows results of relative area as a function of *dB*/*dt* thresholds. For all cases, the more intense *dB*/*dt* variations,

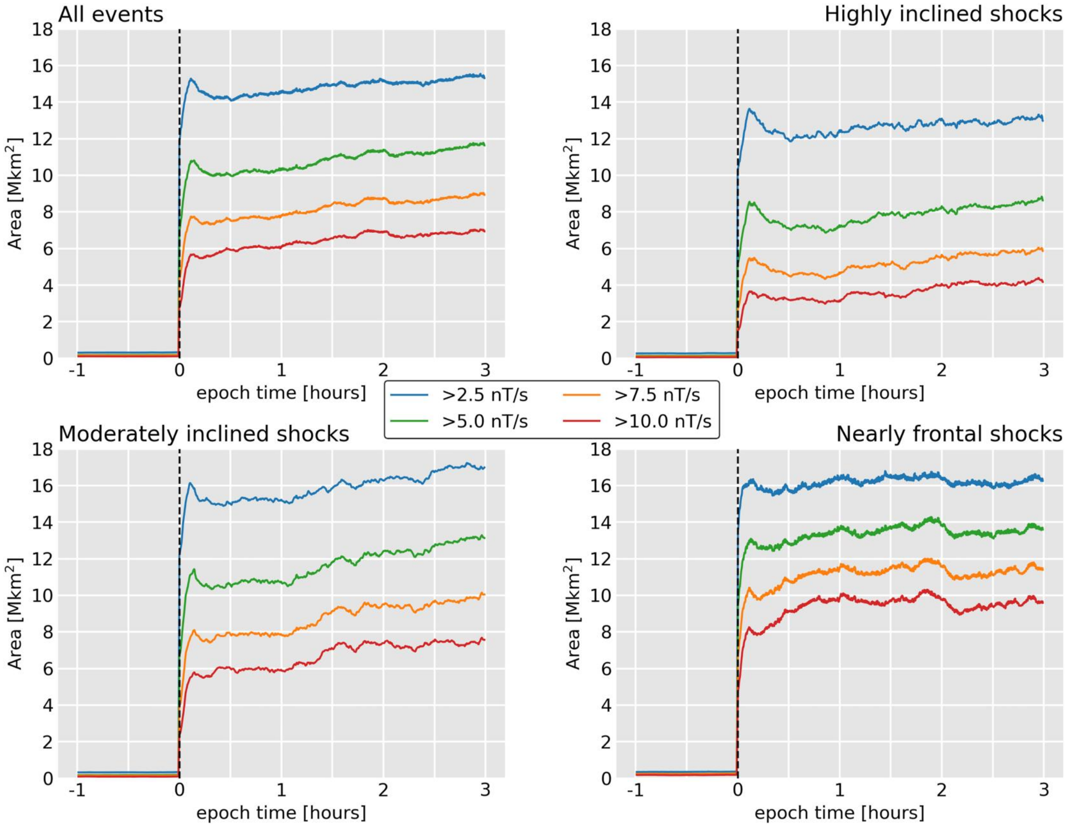

Figure 10. Temporal superposed epoch analyses of absolute geographic areas with dB/dt variations surpassing the following thresholds: blue, dB/dt > 2.5 nT/s; green, dB/dt > 5.0 nT/s; orange, dB/dt > 7.5 nT/s; and red, dB/dt > 10.0 nT/s. The zero epoch time is the shock impact time on the magnetosphere.

the smaller the area coverage. HIS results show $dB/dt \sim 5$ nT/s appearing in nearly 40% of the total geographic area, and $dB/dt \sim 7.5$ nT/s covering ~18% of the total geographic area. In this case, the maximum dB/dt variations observed are shortly lower than 10 nT/s. As previously seen in Figure 8, geographic area coverages for all cases and in the MIS case are very similar, as seen in their slopes, with maximum dB/dt variations near 15 nT/s. In this case, dB/dt variations around 5 nT/s have an area coverage slightly higher than 60%. Maximum dB/dt levels of near 25 nT/s are observed in the NFS case, with 5 nT/s and 10 nT/s appearing in around 88% and 55% of the total geographic area, respectively. Also, it is interesting to note that the rate of change is the highest for HIS, and then is followed by ALL/MIS and NFS. This feature shows that ground dB/dt variations cover relatively more areas in the shock inclination categories with small shock inclinations.

Temporal superposed epoch analyses of absolute geographic area coverages with different dB/dt thresholds (not MLT-filtered) are shown in Figure 10. The dB/dt thresholds are >2.5 nT/s (blue); >5 nT/s (green); >7.5 nT/s (orange); and >10 nT/s (red). In all panels, the vertical dashed black lines indicate the shock impact onset as the zero-epoch time. There is a sharp increase in area coverage in all cases and dB/dt thresholds, which indicate sudden dB/dt variations caused by the shock impacts. Additionally, the difference between absolute area coverages is more evident with higher dB/dt variation thresholds, being the highest for $dB/dt > 10$ nT/s in the case of NFS. General results show that (a) the more intense the dB/dt variation, the smaller the area coverage, and (b) individual area coverages for each dB/dt threshold is higher in the shock inclination categories with smaller shock impact angles.

Since SECS currents are computed at the altitude of 100 km and AMPERE currents are defined at 780 km altitudes, the former current must be mapped to the latter current altitudes for comparisons. According to Ampère's law (Jackson, 1999), the field-aligned component (parallel to the magnetic field) of the current is given by

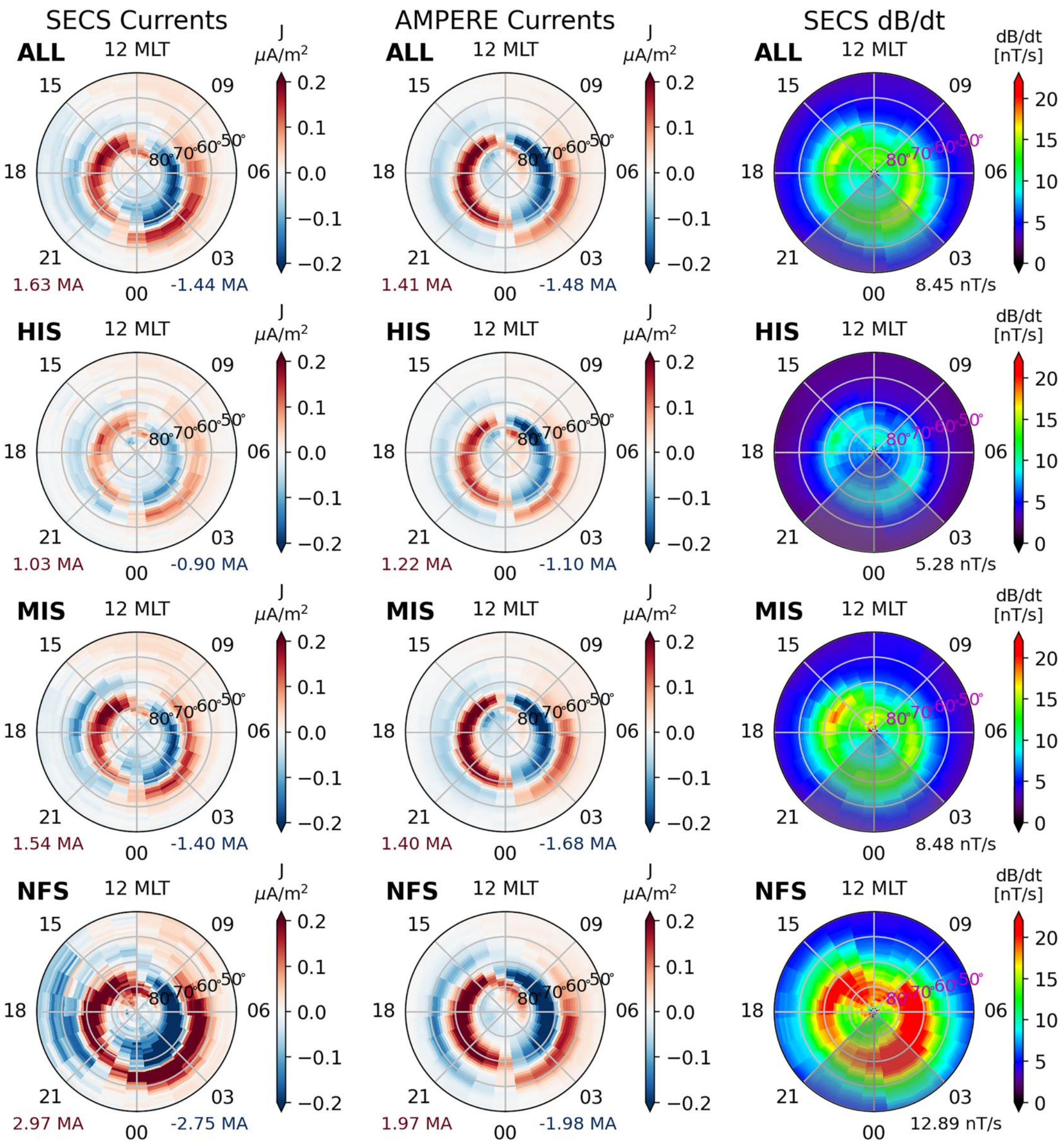

Figure 11. Left column: SECS current densities; middle column: AMPERE Birkeland current densities; and right column: SECS ground d*B*/d*t* variations. The highlighted areas in the d*B*/d*t* panels represent areas of interest located around the midnight magnetic local time terminator (MLT ≤ 03 hr; MLT ≥ 21 hr).

$$J\| = \frac{1}{\mu_0}\frac{\mathbf{B}\cdot(\mathrm{curl}\,\mathbf{B})}{\mathrm{B}}. \tag{5}$$

Assuming the parallel current flows along a flux tube without any diversion, the term $\mathbf{B}\cdot(\mathrm{curl}\,\mathbf{B})$ is conserved and the SECS currents can be mapped from 100 to 780 km altitudes according to the expression (Donovan, 1993)

$$J_{780} = \frac{B_{100}}{B_{780}} J_{100}, \tag{6}$$

where the magnetic field magnitudes shown in the above equation are computed with the IGRF model.

Figure 11 shows dial plots of SECS current densities (in μA/m^2, left column), northern hemisphere AMPERE Birkeland current densities (in μA/m^2, middle column), and SECS ground *dB*/*dt* variations (right column) for the shock-induced substorms. Both SECS data are plotted for 237 events (2008–2022), whereas AMPERE data are plotted for 201 events (2010–2022). From top to bottom, the first row is for ALL events; second row, HIS; third row, MIS, and fourth row, NFS. The bin sizes for all dial plots is of 1° and 1 hr for MLAT and MLT, respectively. In order to make a more precise comparison between the SECS and AMPERE currents, a 2-min filter was passed on the 10-s resolution SECS data to match the time resolution of the AMPERE data (2 min). The numerical values displayed on the bottom corners of the current panels indicate the integrated current flowing into (blue color) and out of (red color) the MI system during the substorm interval.

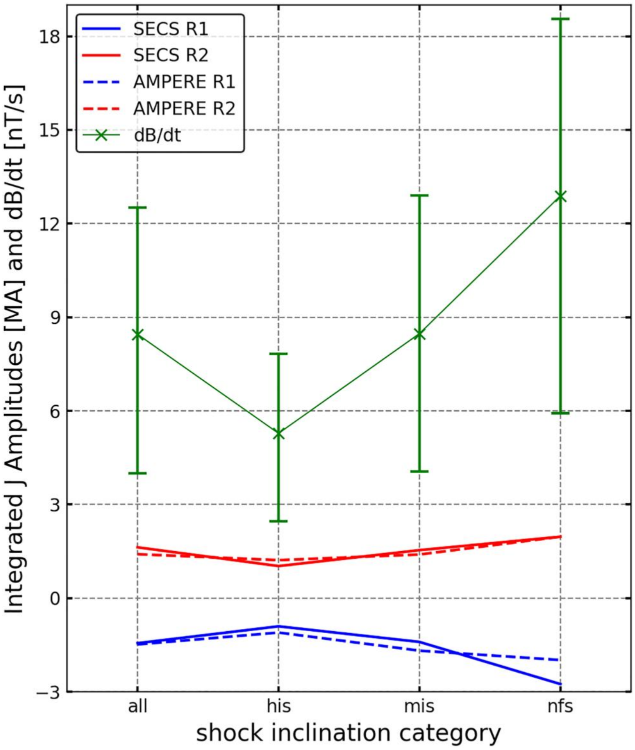

Figure 12. Summary of the statistical results of the substorm-time mean integrated values of SECS and AMPERE Region 1 (R1) and Region 2 (R2) currents shown in the left and middle columns in Figure 11 for all shock orientation groups. Additionally, d*B*/d*t* statistical results (crosses, mean values; error bars: lower limits, 20% quartile; upper limits, 80% quartile) for all shock inclination categories are shown. The d*B*/d*t* data are MLT-filtered around the magnetic midnight terminator to account for substorm activity.

Comparisons between SECS and AMPERE currents show some moderate agreements and striking differences. For example, both data sets capture R1 and R2 current patterns reasonably well, but it seems like SECS patterns are off in comparison to AMPERE patters by 1 hr of MLT. In addition, both currents appear to agree with respect to the mean integrated current values shown in the left (R1, blue) and right (R2, red) bottom corners of each panel, except for the NFS case, with NFS R1 and R2 currents being more intense in the SECS case. Additionally, the NFS case shows a well-defined and intense current density structure in the post-midnight/dawn sector in the SECS case, which does not clearly appear in the AMPERE case. Figure 12 summarizes the comparisons between the total integrated R1 and R2 currents (blue and red lines) for both SECS and AMPERE data sets during the time interval of interest.

In Figure 11, the results of ground SECS *dB*/*dt* variations for all events show values near 10 nT/s from polar regions to 70° in the dawn-noon sector, to 65°, from MLT ~ 12 hr to around the magnetic midnight, and to 60° in the post-midnight sector (00 hr < MLT < 03 hr). Very similar results are seen in the MIS case, with small patches showing *dB*/*dt* enhancements near 20 nT/s at MLAT = 70° (pre-dusk sector), and very high latitudes in the cusp. The case with HIS shows the weakest results, with *dB*/*dt* variations mostly smaller than 10 nT/s. Most concentrations of *dB*/*dt* variations near 8 nT/s around 70°–75° magnetic latitudes, with some enhancements in the cusp. The case with NFS is the most geoeffective. Ground *dB*/*dt* variations of around 10 nT/s reach magnetic latitudes as low as 55° in the midnight-dawn sector. Very intense *dB*/*dt* variations larger than 20 nT/s around MLAT = 70°, with a thicker latitudinal band (65°–75°) from 00 to 06 hr magnetic local time. These *dB*/*dt* variations agree with SECS and AMPERE results for the currents, particularly in the NFS case. The green crosses of Figure 12 shows the mean MLT-filtered *dB*/*dt* levels as a function of shock inclination category shown in Figure 11 (right column). The green error bars show the upper (80%) and lower (20%) percentiles of *dB*/*dt* variations. The HIS-MIS-NFS curve (along with both lower and upper percentiles) shows an almost linear increase, with the MIS value being very close to the ALL value.

3.4. Inter-Hemispheric Asymmetries of Field-Aligned Currents: AMPERE Data

Figure 13 shows AMPERE Birkeland currents observed from the northern hemisphere (left column) and southern hemisphere (right) column, with the same format and resolutions as shown in the left and middle columns in Figure 11. All panels show that the field-aligned currents present well-defined spatial current structures. The current enhancements in the southern hemisphere are more intense in the shock inclination groups with shocks with smaller impact angles, similarly to what happens in the northern hemisphere. However, the integrated Birkeland currents are more intense in the northern hemisphere than in the southern hemisphere in all cases. As summarized in Figure 14, both northern hemisphere R1 (solid blue line) and R2 (solid red line) currents are stronger than the southern hemisphere R1 (dashed blue line) and R2 (dashed red line) currents. This pattern is seen in all shock inclination categories.

Similarly to what was reported for SECS currents (Figure 5), Figure 15 shows temporal superposed epoch analysis results for the AMPERE Birkeland currents in the northern (left columns) and southern (right column)

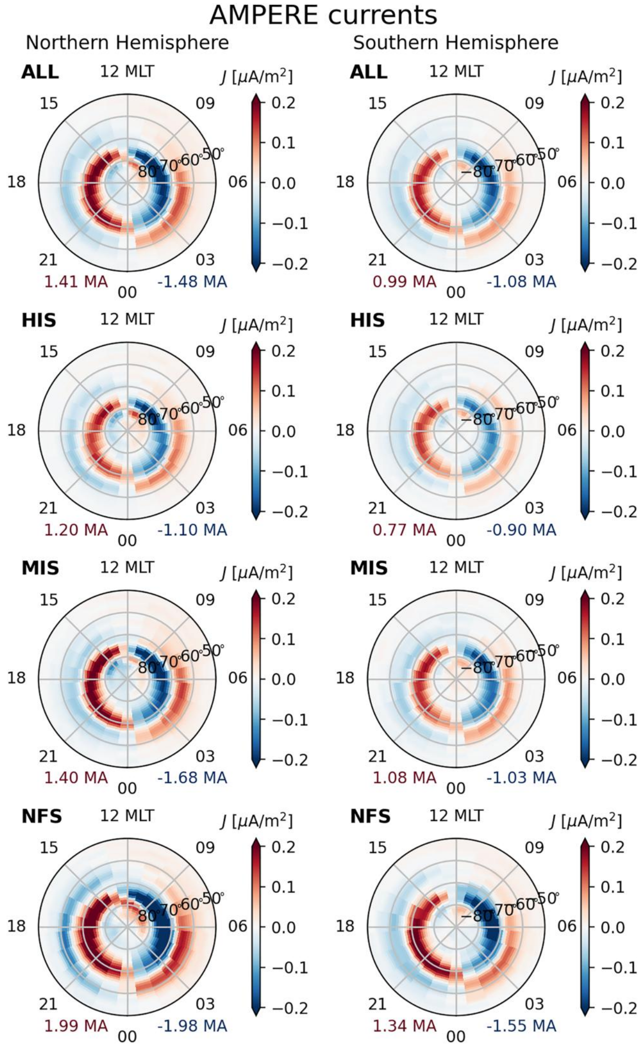

Figure 13. Superposed epoch analysis of AMPERE Birkeland currents in a time interval of 10 min to 3 hours after shock impact, in the northern hemisphere (left column), and southern hemisphere (right column). From top to bottom: first row, all events; second row, highly inclined shocks; third row, moderately inclined shocks; and fourth row, nearly frontal shocks. Downward (negative) currents are represented by blue colors, whereas upward (positive) currents are represented by red colors. The numbers in the bottom left and right portions of each panel indicate the integrated mean current, in MA, flowing into and out of the magnetosphere-ionosphere system, respectively.

hemisphere. The data is not MLT-filtered in this case. Results of mean (thick lines), 20%, and 80% percentiles indicate that the smaller the shock impact angle, the more intense the field aligned current enhancement. However, the northern hemispheric currents are more intense than the southern hemispheric currents.

4. Discussion

The main goal of this paper is to investigate how IP shock impact angles control the subsequent ionospheric current response and ground *dB*/*dt* variations during substorm times. We followed the work of Oliveira et al. (2021), who performed a comparative study of the same topic with similar data using two similarly strong IP shocks, but one being nearly frontal, and the other, highly inclined. The authors concluded that the nearly frontal shock caused (a) more intense and well-defined ionospheric current amplitudes; (b) more intense ground *dB*/*dt* variations that reached lower latitudes; and (c) larger geographic coverages with regions showing intense *dB*/*dt* variations surpassing 1.5 nT/s and 5 nT/s, which could cause deleterious consequences to ground infrastructure (Molinski, 2002; Pulkkinen et al., 2013). Then, we addressed Oliveira et al. (2021)'s results with a superposed epoch analysis and statiscal study investigation with more than 200 IP shocks with different inclinations.

However, while ground *dB*/*dt* variations can be used as a metric, there is a significant spectral dependence of the resulting actual GICs on *dB*/*dt* due to its interaction with non-uniform conductivity structures and conductivity layers in the ground that is not fully captured by *dB*/*dt* (Kelbert & Lucas, 2020; Juusola et al., 2020; X. Wang et al., 2021). However, we believe this issue does not affect the results of this work.

As shown in Figure 4, SECS currents are more intense in the category of shocks with small inclinations, which is supported by previous works with observations and simulations (Guo et al., 2005; Oliveira & Raeder, 2014; Samsonov et al., 2015; Selvakumaran et al., 2017; Shi et al., 2019). Perhaps the most striking difference between SECS current densities and AMPERE Birkeland current densities (Figure 11) is a very clear and well-defined Harang discontinuity structure (Harang, 1946) observed around MLT = 23 hr for the SECS NFS case, which does not clearly appear in the AMPERE NFS case. This effect was reported before with SECS current data (Oliveira et al., 2021; Weygand, 2021), and it is clearly seen in the NFS panel of Figure 4. The lack of a Harang discontinuity structure in the AMPERE case is presumably due to a possible current smoothing due to the spherical harmonics procedure used to compute the currents (Waters et al., 2020) or the way the data was organized in this work. On the other hand, Coxon et al. (2017) were able to show a clear post-midnight Harang discontinuity when AMPERE Birkeland current data was superposed at the onset of more than 1,000 substorms including events not necessarily triggered by shock impacts.

The geographic maps of North America and Greenland (Figure 8) show that even shocks in the HIS category with ground *dB*/*dt* variations near 10 nT/s in mid- and high-latitude Canada can pose significant risks to ground conductors. GICs associated with such ground *dB*/*dt* variation thresholds can be highly detrimental to power transmission lines and oil/gas pipelines (Molinski, 2002; Pulkkinen et al., 2013). For the ALL and MIS categories, *dB*/*dt* variations around 10 nT/s can be seen close to the Canadian border with the United States, whereas *dB*/*dt* variations near 15 nT/s is observed in mid-latitude Canada. In addition, in the NFS case, *dB*/*dt* variations are very intense in mid-latitude Canada (>20 nT/s), and values near 10 nT/s are observed close to MLAT = 50°. These results were observed by Oliveira et al. (2021) during two super substorms triggered by shocks with

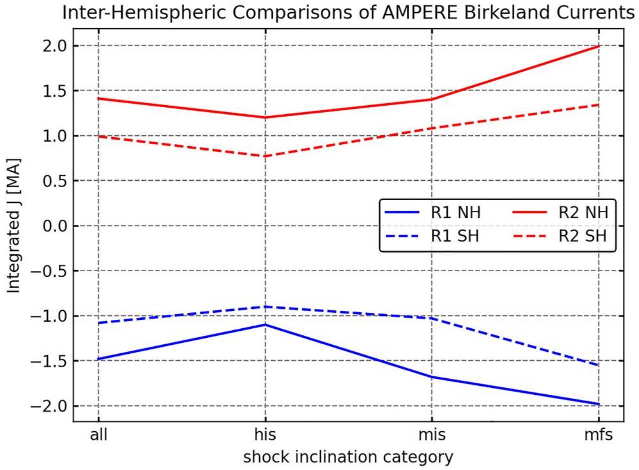

Figure 14. Summary of the statistical results of Region 1 (R1, blue) and Region 2 (R2, red) Birkeland currents shown in Figure 13 for the northern hemisphere (solid lines) and southern hemisphere (dashed lines).

different inclinations. Weygand (2021) also showed similar *dB*/*dt* variations during isolated substorms without discrimination of the substorm triggering mechanism. As a result, as pointed out by Oliveira (2023a), space weather forecasting tools should focus on tracking IP shocks that are predicted to impact the magnetosphere nearly head-on for predicting high-risk *dB*/*dt* variations at magnetic latitudes lower than 70°. In addition, a visual inspection of Figure 8 and the curves in Figures 9, 10, and 12 show that, based on *dB*/*dt* responses, a typical solar wind shock normal vector has moderate inclination with ∼20°–40° deviations with respect to the Sun-Earth line, which are more frequently observed at 1 AU (Echer et al., 2023; Kilpua et al., 2015; Oh et al., 2007; Oliveira, 2023a; Oliveira & Raeder, 2015; Rudd et al., 2019).

C. Wang et al. (2006) and Rudd et al. (2019) showed that rise times of positive shock-triggered sudden impulses recorded by worldwide ground magnetometers are shorter for nearly head-on shocks. Oliveira et al. (2018) showed that ground *dB*/*dt* variations are more intense at high latitudes when triggered by nearly frontal shocks with high speeds. In addition, Xu et al. (2020) used north-south conjugated ground station magnetometer data to show that the stations in the hemisphere that is first impacted by the shock indicate the first and more intense ground *dB*/*dt* response. As shown in Figure 10, the enhancements in absolute area coverages are larger and sharper in the shock inclination categories with smaller shock impact angles, which agrees with previous observations described above. These results agree with ground magnetic field response to shocks with different inclinations since more frontal shocks compress the magnetosphere more symmetrically and enhances magnetospheric and ionospheric currents more effectively in comparison to inclined shocks (Oliveira, 2023a; Oliveira & Samsonov, 2018).

The intense post-midnight/dawn currents and *dB*/*dt* enhancements seen in Figure 11 (NFS case) agree with observations reported by Ohtani et al. (2018) of R1 and R2 currents in that MLT region during intense magnetic storms and by Shi et al. (2019) for shocks. In addition, such post-midnight *dB*/*dt* enhancements may be due to intensifications of the dawnside westward auroral electrojet current. According to Ohtani et al. (2023), the dawnside westward auroral electrojet current can be intensified during periods of high dynamic pressure enhancements and energetic electrons precipitating from the plasmasheet into the dawn sector leading to increased conductance levels there (Newell et al., 2009; Wing et al., 2014). Additionally, Madelaire et al. (2022) suggested that dynamic pressure enhancements caused by solar wind discontinuities intensify the partial ring current during southward IMF periods leading in turn to intense geomagnetic field perturbations at mid and low latitudes. As a result, these processes enhance field-aligned currents, particularly R2 currents, and magnetopause currents at mid and low latitudes, leading to high-level *dB*/*dt* variations observed in such unusually low latitudes (nearly MLAT = 50°).

Inter-hemispheric asymmetries in AMPERE Birkeland currents are observed in Figures 13–15. In general, the northern hemisphere response is more intense than the southern hemisphere response. Observations of more intense Poynting flux enhancements in the northern hemisphere support these findings (Knipp et al., 2021; Oliveira et al., 2022; Pakhotin et al., 2021). This is explained by a larger offset between the magnetic quasi-dipole high-latitude dips with respect to the Earth's center in the southern hemisphere in comparison to the northern hemisphere (Constable et al., 2016; Laundal et al., 2017; Livermore et al., 2020). The offsets between the Earth's rotation axes and the positions of the highest magnetic inclination (±90° for the northern and southern hemispheres, respectively), calculated with the Haversine formula (Gade, 2010) and the IGRF model, are shown in Figure 16. The highlighted gray area indicates the time investigated in this study. As noted by Pakhotin et al. (2021), the southern hemisphere auroral oval is generally more in darkness in comparison to the northern hemisphere auroral oval, which may affect conductances and auroral electrojets more weakly in the southern hemisphere. Although not investigated in this paper, ionospheric conductances, seasons, and IMF B_y may also play a role in determining inter-hemispheric asymmetries in ground magnetic field response (Hartinger et al., 2017; Oliveira et al., 2023; Pilipenko et al., 2020; Weygand et al., 2022). Similar inter-hemispheric asymmetries in AMPERE Birkeland currents were also reported by Shi et al. (2019) with currents enhanced by shocks with different inclinations, and by Coxon et al. (2016) with currents observed in the period 2010–2015

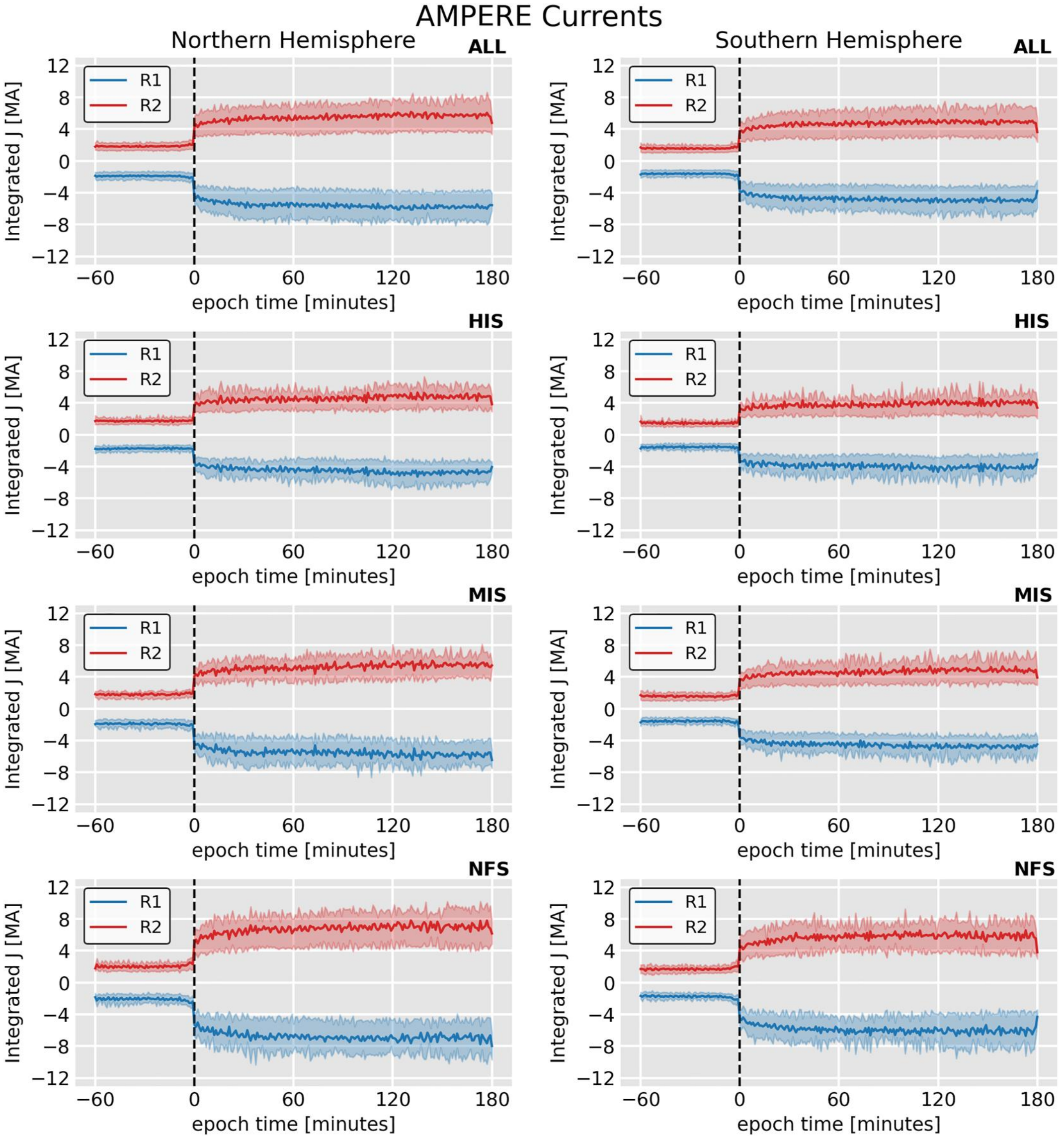

Figure 15. Superposed epoch analysis results of AMPERE current time series for the four shock categories, from top to bottom: all events, first row; highly inclined shocks, second row; moderately inclined shocks, third row; and nearly frontal shocks, fourth row. The first column is for the northern hemisphere, whereas the right column is for the southern hemisphere. Blue colors represent downward currents, while red colors indicate upward currents. The colored shaded areas correspond to the lower (20%) and upper (80%) quartiles.

during general conditions. Although the shock impact angle effects are present in both hemispheres, AMPERE Birkeland currents are more intense in the northern hemisphere for all shock inclination categories.

5. Summary and Conclusions

In this study, we used 237 events from a list of 603 IP shocks to investigate ionospheric current and ground *dB*/*dt* responses to shock impacts with different inclinations on the magnetosphere. Data from large ground magnetometer arrays located in North America from Alaska to Labrador, Colorado to Nunavut, and on Greenland's west coast were used in the investigation. The Spherical Elementary Current System (SECS) technique was applied to the data, and ionospheric current amplitudes (SECS currents) were computed. Then, the Biot-Savart law was applied to the SECS currents and ground *dB*/*dt* variations were obtained. Geographic maps of the currents and field variations as a function of shock impact angles were constructed. Additionally, field-aligned current

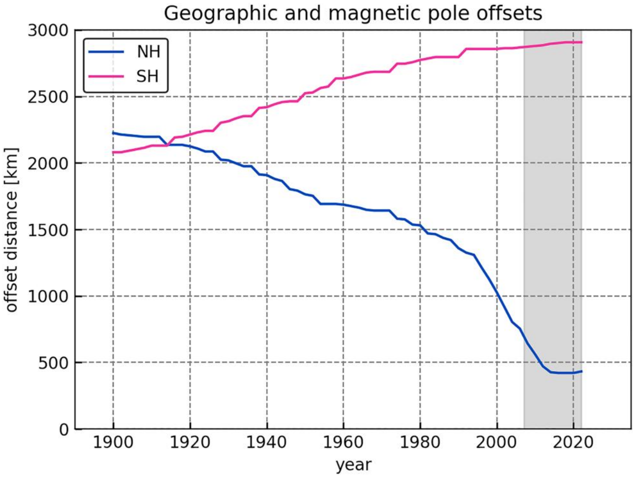

Figure 16. Offset distance between the Earth's rotation and the geographic position of the highest magnetic inclination, ±90° in the northern hemisphere (blue line) and southern hemisphere (pink line). The Haverside equation and the IGRF model were used in the calculations.

densities from AMPERE were used as a supporting data set for comparison with the SECS currents and independent inter-hemispheric comparisons.

The main findings of this work can be summarized as follows:

1. Typical ground *dB*/*dt* variations (5–10 nT/s) are triggered by moderately inclined shocks with shock impact angles in the range $140^\circ < \theta_{x_n} < 160^\circ$. This is clearly seen in Figures 8 and 9.
2. In general, nearly frontal shocks lead to more intense and more well-spatially defined current amplitudes in the ionosphere. This general result confirms the results of the comparative case study reported by Oliveira et al. (2021).
3. A well spatially defined Harang discontinuity is observed in the northern hemisphere with SECS currents in the pre-midnight sector (MLT ~ 23 hr). This occurs more clearly in the nearly frontal shock category and is not clearly shown in the AMPERE data.
4. Geographic maps of ground *dB*/*dt* variations show that the more frontal the shock impact, the more intense and the lower the equatorial extent of the subsequent ground *dB*/*dt* variations. In addition, these maps show that intense *dB*/*dt* variation thresholds (>5 nT/s and >10 nT/s), appear, respectively, in nearly 85% and 50% of the geographic areas investigated. These results also agree with the comparative study of Oliveira et al. (2021).
5. SECS currents and ground *dB*/*dt* variations are strongly enhanced in the midnight-dawn sector particularly in the case of the nearly frontal shocks. This is due to high intensifications and equatorward extensions of Region 2 currents in that region. This result agrees with previous observations of dawnside field-aligned currents, current wedges, and westward auroral electrojet during IP shocks and magnetic storms (Ohtani et al., 2018, 2023; Shi et al., 2019).
6. AMPERE field-aligned currents in the northern hemisphere generally agree with SECS currents in the sense that, the more frontal the shock impact, the more intense the resulting current. As a byproduct result of this investigation, we found that integrated field-aligned currents observed by AMPERE are more intense in the northern hemisphere in comparison to currents observed in the southern hemisphere. These results agree with inter-hemispheric asymmetries obtained from Poynting flux enhancements computed with magnetic field observations in low-Earth orbit (Knipp et al., 2021; Oliveira et al., 2022; Pakhotin et al., 2021), as well as with previous of AMPERE Birkeland currents (Coxon et al., 2016, 2022; Shi et al., 2019).

Furthermore, the findings of this work have significant implications to future space weather investigations focusing on GIC enhancements occurring during shock-induced substorms. More specifically, forecasters should predict and track impacts of nearly frontal shocks on the Earth's magnetosphere. Additionally, as pointed out by Oliveira (2023a), it is strongly recommended modelers simulate the impacts of shocks with different normal orientations on the magnetosphere to investigate, in particular, the subsequent GIC enhancements during asymmetric magnetospheric compressions. As reported by Welling et al. (2021), ground *dB*/*dt* variations were highly intensified and reached low equatorial latitudes as a result of the impact of a perfect coronal mass ejection with purely frontal normal orientation, which is a very particular case. This is supported by results shown in Figure 1 and by many other works (Kilpua et al., 2015; Oh et al., 2007; Oliveira, 2023a; Oliveira & Samsonov, 2018; Rudd et al., 2019), meaning that most shocks observed at 1 AU have moderate inclinations of ~30–40° with respect to the line connecting the Earth and the Sun.

Data Availability Statement

The interplanetary shock data base can be downloaded from the Zenodo repository described in Oliveira (2023c). The SECS data (ionospheric current amplitudes and ground *dB*/*dt* variations) are publicly available at the Virtual Magnetospheric Observatory website (http://vmo.igpp.ucla.edu/data1/SECS/). The AMPERE Birkeland current data were downloaded from https://ampere.jhuapl.edu. Links to individual ground magnetometer data are available in the Supporting Information S1.

Acknowledgments

DMO, JMW, and EZ thank NASA's Heliophysics Guest Investigators-Open (HGIO) program for the financial support through Grant 80NSSC22K0756. JCC was supported by Science and Technology Facilities Council Ernest Rutherford Fellowship ST/V004883/1.

References

Abraham-Shrauner, B. (1972). Determination of magnetohydronamic shock normals. *Journal of Geophysical Research*, *77*(4), 736–739. https://doi.org/10.1029/JA077i004p00736

Akasofu, S.-I. (1981). Magnetospheric substorms: A newly emerging model. *Planetary and Space Science*, *29*(10), 1069–1078. https://doi.org/10.1016/0032-0633(81)90004-0

Alken, P., Thébault, E., Beggan, C. D., Amit, H., Aubert, J., Baerenzung, J., et al. (2021). International geomagnetic reference field: The thirteenth generation. *Earth Planets and Space*, *73*(49), 49. https://doi.org/10.1186/s40623-020-01288-x

Alves, M. V., Echer, E., & Gonzalez, W. D. (2011). Geoeffectiveness of solar wind interplanetary magnetic structures. *Journal of Atmospheric and Solar-Terrestrial Physics*, *73*(11–12), 1380–1384. https://doi.org/10.1016/j.jastp.2010.07.024

Amm, O., Engebretson, M. J., Hughes, T., Newitt, L., Viljanen, A., & Watermann, J. (2002). A traveling convection vortex event study: Instantaneous ionospheric equivalent currents, estimation of field-aligned currents, and the role of induced currents. *Journal of Geophysical Research*, *107*(A11), SIA1-1–SIA1-11. https://doi.org/10.1029/2002JA009472

Amm, O., & Viljanen, A. (1999). Ionospheric disturbance magnetic field continuation from the ground to the ionosphere using spherical elementary current systems. *Earth Planets and Space*, *51*(6), 431–440. https://doi.org/10.1186/BF03352247

Anderson, B. J., Takahashi, K., & Toth, B. A. (2000). Sensing global Birkeland currents with Iridium® engineering magnetometer data. *Geophysical Research Letters*, *27*(24), 4045–4048. https://doi.org/10.1029/2000GL000094

Andréeová, K., & Přech, L. (2007). Propagation of interplanetary shocks into the Earth's magnetosphere. *Advances in Space Research*, *40*(12), 1871–1880. https://doi.org/10.1016/j.asr.2007.04.079

Baker, K. B., & Wing, S. (1989). A new magnetic coordinate system for conjugate studies at high latitudes. *Journal of Geophysical Research*, *94*(A7), 9139–9143. https://doi.org/10.1029/JA094iA07p09139

Bargatze, L. F., Baker, D. N., McPherron, R. L., & Hones, E. W., Jr. (1985). Magnetospheric impulse response for many levels of geomagnetic activity. *Journal of Geophysical Research*, *90*(A7), 6387–6394. https://doi.org/10.1029/JA090iA07p06387

Belakhovsky, V. B., Pilipenko, V., Sakharov, Y. A., Lorentsen, D. L., & Samsonov, S. N. (2017). Geomagnetic and ionospheric response to the interplanetary shock on January 24, 2012. *Earth Planets and Space*, *69*(105), 1–25. https://doi.org/10.1186/s40623-017-0696-1

Burch, J. L. (1972). Preconditions for the triggering of polar magnetic substorms by storm sudden commencements. *Journal of Geophysical Research*, *77*(28), 5629–5632. https://doi.org/10.1029/JA077i028p05629

Burlaga, L. F. (1971). Hydromagnetic waves and discontinuities in the solar wind. *Space Science Reviews*, *12*(5), 600–657. https://doi.org/10.1007/BF00173345

Chao, J. K., & Lepping, R. P. (1974). A correlative study of SSC's, interplanetary shocks, and solar activity. *Journal of Geophysical Research*, *79*(13), 1799–1807. https://doi.org/10.1029/JA079i013p01799

Cole, K. D. (1962). Joule heating of the upper atmosphere. *Australian Journal of Physics*, *15*(2), 223–235. https://doi.org/10.1071/PH620223

Constable, C., Korte, M., & Panovska, S. (2016). Persistent high paleosecular variation activity in southern hemisphere for at least 10 000 years. *Earth and Planetary Science Letters*, *453*, 78–86. https://doi.org/10.1016/j.epsl.2016.08.015

Cowley, S. W. H. (2000). Magnetosphere-ionosphere interactions: A tutorial review. In S. Ohtani, R. Fujii, M. Hesse, & R. L. Lysak (Eds.), *Magnetospheric current systems*, *Geophysical monograph series* (Vol. 118, pp. 91–106). American Geophysical Union. https://doi.org/10.1029/GM118p0091

Coxon, J. C., Chisham, G., Freeman, M. P., Anderson, B. J., & Fear, R. C. (2022). Distributions of Birkeland current density observed by AMPERE are heavy-tailed or long-tailed. *Journal of Geophysical Research: Space Physics*, *127*(2), e2021JA029801. https://doi.org/10.1029/2021JA029801

Coxon, J. C., Milan, S. E., & Anderson, B. J. (2018). A review of Birkeland current research using AMPERE. In A. Keiling, O. Marghitu, & M. Wheatland (Eds.), *Electric current in geospace and beyond*, *Geophysical monograph series* (Vol. 235, pp. 259–278). American Geophysical Union. https://doi.org/10.1002/9781119324522.ch16

Coxon, J. C., Milan, S. E., Carter, J. A., Clausen, L. B. N., Anderson, B. J., & Korth, H. (2016). Seasonal and diurnal variations in AMPERE observations of the Birkeland currents compared to modeled results. *Journal of Geophysical Research: Space Physics*, *121*(5), 4027–4040. https://doi.org/10.1002/2015JA022050

Coxon, J. C., Rae, I. J., Forsyth, C., Jackman, C. M., Fear, R. C., & Anderson, B. J. (2017). Birkeland currents during substorms: Statistical evidence for intensification of Regions 1 and 2 currents after onset and a localized signature of auroral dimming. *Journal of Geophysical Research: Space Physics*, *122*(6), 6455–6468. https://doi.org/10.1002/2017JA023967

Davis, T. N., & Sugiura, M. (1966). Auroral electrojet activity index AE and its universal time variations. *Journal of Geophysical Research*, *71*(3), 785–801. https://doi.org/10.1029/JZ071i003p00785

Donovan, E. F. (1993). Modeling the magnetic effects of field-aligned currents. *Journal of Geophysical Research*, *98*(A8), 13529–13543. https://doi.org/10.1029/93JA00603

Echer, E. (2019). Solar wind and interplanetary shock parameters near Saturn's orbit (∼10 AU). *Planetary and Space Science*, *165*, 210–220. https://doi.org/10.1016/j.pss.2018.10.006

Echer, E., Alves, M. V., & Gonzalez, W. D. (2004). Geoefectiveness of interplanetary shocks during solar minimum (1995) and solar maximum (2000). *Solar Physics*, *221*(2), 361–380. https://doi.org/10.1023/B:SOLA.0000035045.65224.f3

Echer, E., de Lucas, A., Hajra, R., de Souza Franco, A. M., Bolzan, M. J. A., & do Nascimento, L. E. S. (2023). Geomagnetic activity following interplanetary shocks in solar cycles 23 and 24. *Brazilian Journal of Physics*, *53*(79), 1–13. https://doi.org/10.1007/s13538-023-01294-w

Fiori, R. A. D., Boteler, D. H., & Gillies, D. M. (2014). Assessment of GIC risk due to geomagnetic sudden commencements and identification of the current systems responsible. *Space Weather*, *12*(1), 76–91. https://doi.org/10.1002/2013SW000967

Freeman, M. P., Forsyth, C., & Rae, I. J. (2019). The influence of substorms on extreme rates of change of the surface horizontal magnetic field in the United Kingdom. *Space Weather*, *17*(6), 827–844. https://doi.org/10.1029/2018SW002148

Freeman, M. P., & Morley, S. K. (2004). A minimal substorm model that explains the observed statistical distribution of times between substorms. *Geophysical Research Letters*, *31*(12), L12807. https://doi.org/10.1029/2004GL019989

Fukushima, N. (1994). Some topics and historical episodes in geomagnetism and aeronomy. *Journal of Geophysical Research*, *99*(A10), 19113–19142. https://doi.org/10.1029/94JA00102

Gade, K. (2010). A non-singular horizontal position representation. *Journal of Navigation*, *63*(3), 295–417. https://doi.org/10.1017/S0373463309990415

Gjerloev, J. W., Hoffman, R. A., Friel, M. M., Frank, L. A., & Sigwarth, J. B. (2004). Substorm behavior of the auroral electrojet indices. *Annales Geophysicae*, *22*(6), 2135–2149. https://doi.org/10.5194/angeo-22-2135-2004

Guo, X.-C., Hu, Y.-Q., & Wang, C. (2005). Earth's magnetosphere impinged by interplanetary shocks of different orientations. *Chinese Physics Letters*, *22*(12), 3221–3224. https://doi.org/10.1088/0256-307X/22/12/067

Hajra, R. (2021). Variation of the interplanetary shocks in the inner heliosphere. *The Astrophysical Journal*, *917*(2), 91. https://doi.org/10.3847/1538-4357/ac0897

Harada, Y., Gurnett, D. A., Kopf, A. J., Halekas, J. S., Ruhunusiri, S., Lee, C. O., et al. (2017). Dynamic response of the Martian ionosphere to an interplanetary shock: Mars Express and MAVEN observationsmihalov. *Geophysical Research Letters*, *44*(18), 9116–9123. https://doi.org/10.1002/2017GL074897

Harang, L. (1946). The mean field of disturbance of polar geomagnetic storms. *Terrestrial Magnetism and Atmospheric Electricity*, *51*(3), 353–380. https://doi.org/10.1029/TE051i003p00353

Hartinger, M. D., Xu, Z., Clauer, C. R., Yu, Y., Weimer, D. R., Kim, H., et al. (2017). Associating ground magnetometer observations with current or voltage generators. *Journal of Geophysical Research: Space Physics*, *122*(7), 7130–7141. https://doi.org/10.1002/2017JA024140

Jackson, J. D. (1999). *Classical electrodynamics* (3rd ed.). John Wiley &, Inc.

Jeffrey, A., & Taniuti, T. (1964). *Nonlinear wave propagation*. Academic Press.

Juusola, L., Heikki Vanhamäki, A. V., & Smirnov, M. (2020). Induced currents due to 3D ground conductivity play a major role in the interpretation of geomagnetic variations. *Annales Geophysicae*, *30*(5), 983–998. https://doi.org/10.5194/angeo-38-983-2020

Kalmoni, N. M. E., Rae, I. J., Watt, C. E. J., Murphy, K. R., Samara, M., Michell, R. G., et al. (2018). A diagnosis of the plasma waves responsible for the explosive energy release of substorm onset. *Nature Communications*, *9*(4806), 4806. https://doi.org/10.1038/s41467-018-07086-0

Kamide, Y., & Nakamura, R. (1996). The convection electrojet and the substorm electrojet. *Annales Geophysicae*, *14*(6), 589–592. https://doi.org/10.1007/s00585-996-0589-2

Kelbert, A., & Lucas, G. M. (2020). Modified GIC estimation using 3-D Earth conductivity. *Space Weather*, *18*(8), e2020SW002467. https://doi.org/10.1029/2020SW002467

Kilpua, E. K. J., Lumme, K., Andréeová, E., Isavnin, A., & Koskinen, H. E. J. (2015). Properties and drivers of fast interplanetary shocks near the orbit of the Earth (1995–2013). *Journal of Geophysical Research: Space Physics*, *120*(6), 4112–4125. https://doi.org/10.1002/2015JA021138

Knipp, D., Kilcommons, L., Hairston, M., & Coley, W. R. (2021). Hemispheric asymmetries in poynting flux derived from DMSP spacecraft. *Geophysical Research Letters*, *48*(17), e2021GL094781. https://doi.org/10.1029/2021GL094781

Krauss, S., Temmer, M., & Vennerstrom, S. (2018). Multiple satellite analysis of the Earth's thermosphere and interplanetary magnetic field variations due to ICME/CIR events during 2003-2015. *Journal of Geophysical Research: Space Physics*, *123*(10), 8884–8894. https://doi.org/10.1029/2018JA025778

Kumar, M. (2009). World geodetic system 1984: A modern and accurate global reference frame. *Marine Geology*, *12*(2), 117–126. https://doi.org/10.1080/15210608809379580

Lamy, L. (2020). Auroral emissions from Uranus and Neptune. *Philosophical Transactions of the Royal Society. Series A*, *378*(2187), 1–17. https://doi.org/10.1098/rsta.2019.0481

Laundal, K. M., Cnossen, I., Milan, S. E., Haaland, S. E., Coxon, J., Pedatella, N. M., et al. (2017). North–South asymmetries in Earth's magnetic field. *Space Science Reviews*, *206*(1–4), 225–257. https://doi.org/10.1007/s11214-016-0273-0

Liu, J., Chakraborty, S., Chen, X., Wang, Z., He, F., Hu, Z., et al. (2023). Transient response of polar-cusp ionosphere to an interplanetary shock. *Journal of Geophysical Research: Space Physics*, *128*(3), e2022JA030565. https://doi.org/10.1029/2022JA030565

Livermore, P. W., Finlay, C. C., & Bayliff, M. (2020). Recent north magnetic pole acceleration towards Siberia caused by flux lobe elongation. *Nature Geoscience*, *13*(5), 387–391. https://doi.org/10.1038/s41561-020-0570-9

Lugaz, N., Farrugia, C. J., Winslow, R. M., Al-Haddad, N., Kilpua, E. K. J., & Riley, P. (2016). Factors affecting the geo-effectiveness of shocks and sheaths at 1 AU. *Journal of Geophysical Research: Space Physics*, *120*(11), 10861–10879. https://doi.org/10.1002/2016JA023100

Madelaire, M., Laundal, K. M., Reistad, J. P., Hatch, S. M., Ohma, A., & Haaland, S. (2022). Geomagnetic response to rapid increases in solar wind dynamic pressure: Event detection and large scale response. *Frontiers in Astronomy and Space Science*, *9*(904620). https://doi.org/10.3389/fspas.2022.904620

Mende, S. B., Harris, S. E., Frey, H. U., Angelopoulos, V., Russell, C. T., Donovan, E., et al. (2008). The THEMIS array of ground-based observatories for the study of auroral substorms. *Space Science Reviews*, *141*(1–4), 357–387. https://doi.org/10.1007/s11214-008-9380-x

Milan, S. E., Clausen, L. B. N., Coxon, J. C., Carter, J. A., Walach, M.-T., Laundal, K., et al. (2017). Overview of solar wind-magnetosphere-ionosphere-atmosphere coupling and the generation of magnetospheric currents. *Space Science Reviews*, *206*(1–4), 547–573. https://doi.org/10.1007/s11214-017-0333-0

Molinski, T. S. (2002). Why utilities respect geomagnetically induced currents. *Journal of Atmospheric and Solar-Terrestrial Physics*, *64*(16), 1765–1778. https://doi.org/10.1016/S1364-6826(02)00126-8

Moritz, H. (2000). Geodetic reference system 1980. *Journal of Geodesy*, *74*(1), 128–133. https://doi.org/10.1007/s001900050278

Mostafavi, P., Burlaga, L. F., Cairns, I. H., Fuselier, S. A., Fraternale, F., Gurnett, D. A., et al. (2022). Shocks in the very local interstellar medium. *Space Science Reviews*, *218*(27), 27. https://doi.org/10.1007/s11214-022-00893-4

Newell, P. T., Sotirelis, T., & Wing, S. (2009). Diffuse, monoenergetic, and broadband aurora: The global precipitation budget. *Journal of Geophysical Research*, *114*(A9), A09207. https://doi.org/10.1029/2009JA014326

Ngwira, C. M., Sibeck, D., Silveira, M. V. D., Georgiou, M., Weygand, J. M., Nishimura, Y., & Hampton, D. (2018). A study of intense local dB/dt variations during two geomagnetic storms. *Space Weather*, *16*(6), 676–693. https://doi.org/10.1029/2018SW001911

Oh, S. Y., Yi, Y., & Kim, Y. H. (2007). Solar cycle variation of the interplanetary forward shock drivers observed at 1 AU. *Solar Physics*, *245*(2), 391–410. https://doi.org/10.1007/s11207-007-9042-2

Ohtani, S., Gjerloev, J. W., Anderson, B. J., Kataoka, R., Troshichev, O., & Watari, S. (2018). Dawnside wedge current system formed during intense geomagnetic storms. *Journal of Geophysical Research: Space Physics*, *123*(11), 9093–9109. https://doi.org/10.1029/2018JA025678

Ohtani, S., Sorathia, K., Merkin, V. G., Frey, H. U., & Gjerloev, J. W. (2023). External and internal causes of the stormtime intensification of the dawnside westward auroral electrojet. *Journal of Geophysical Research: Space Physics*, *128*(10), e2023JA031457. https://doi.org/10.1029/2023JA031457

Oliveira, D. M. (2017). Magnetohydrodynamic shocks in the interplanetary space: A theoretical review. *Brazilian Journal of Physics*, *47*(1), 81–95. https://doi.org/10.1007/s13538-016-0472-x

Oliveira, D. M. (2023a). Geoeffectiveness of interplanetary shocks controlled by impact angles: Past research, recent advancements, and future work. *Frontiers in Astronomy and Space Science*, *10*. https://doi.org/10.3389/fspas.2023.1179279

Oliveira, D. M. (2023b). Interplanetary shock data base. *Frontiers in Astronomy and Space Science*, *10*. https://doi.org/10.3389/fspas.2023.1240323

Oliveira, D. M. (2023c). Interplanetary shock data base (version 1) [Dataset]. Zenodo. https://doi.org/10.5281/zenodo.7991430

Oliveira, D. M., Arel, D., Raeder, J., Zesta, E., Ngwira, C. M., Carter, B. A., et al. (2018). Geomagnetically induced currents caused by interplanetary shocks with different impact angles and speeds. *Space Weather*, *16*(6), 636–647. https://doi.org/10.1029/2018SW001880

Oliveira, D. M., Hartinger, M. D., Xu, Z., Zesta, E., Pilipenko, V. A., Giles, B. L., & Silveira, M. V. D. (2020). Interplanetary shock impact angles control magnetospheric ULF wave activity: Wave amplitude, frequency, and power spectra. *Geophysical Research Letters*, *47*(24), e2020GL090857. https://doi.org/10.1029/2020GL090857

Oliveira, D. M., & Ngwira, C. M. (2017). Geomagnetically induced currents: Principles. *Brazilian Journal of Physics*, *47*(5), 552–560. https://doi.org/10.1007/s13538-017-0523-y

Oliveira, D. M., & Raeder, J. (2014). Impact angle control of interplanetary shock geoeffectiveness. *Journal of Geophysical Research: Space Physics*, *119*(10), 8188–8201. https://doi.org/10.1002/2014JA020275

Oliveira, D. M., & Raeder, J. (2015). Impact angle control of interplanetary shock geoeffectiveness: A statistical study. *Journal of Geophysical Research: Space Physics*, *120*(6), 4313–4323. https://doi.org/10.1002/2015JA021147

Oliveira, D. M., & Samsonov, A. A. (2018). Geoeffectiveness of interplanetary shocks controlled by impact angles: A review. *Advances in Space Research*, *61*(1), 1–44. https://doi.org/10.1016/j.asr.2017.10.006

Oliveira, D. M., Welling, D. T., Kim, H., Gabrielse, C., Reistad, J. P., & Laundal, K. M. (2023). Editorial: Understanding the causes of asymmetries in Earth's magnetosphere-ionosphere system. *Frontiers in Astronomy and Space Science*, *10*. https://doi.org/10.3389/fspas.2023.1173630

Oliveira, D. M., Weygand, J. M., Zesta, E., Ngwira, C. M., Hartinger, M. D., Xu, Z., et al. (2021). Impact angle control of local intense dB/dt variations during shock-induced substorms. *Space Weather*, *19*(12), e2021SW002933. https://doi.org/10.1029/2021SW002933

Oliveira, D. M., & Zesta, E. (2019). Satellite orbital drag during magnetic storms. *Space Weather*, *17*(11), 1510–1533. https://doi.org/10.1029/2019SW002287

Oliveira, D. M., Zesta, E., Delano, K., & Dorelli, J. (2022). Inter-hemispheric comparisons of Poynting flux and particle precipitation during magnetic storms with different intensities. In *Final paper abstract number: SA33A-04. Presented at the 2022 AGU fall meeting (virtual), 12–16 December*.

Pakhotin, I. P., Mann, I. R., Xie, K., Burchill, J. K., & Knudsen, D. J. (2021). Northern preference for terrestrial electromagnetic energy input from space weather. *Nature Communications*, *21*(199), 1–9. https://doi.org/10.1038/s41467-020-20450-3

Patterson, C. J., Wild, J. A., & Boteler, D. H. (2023). Modeling the impact of geomagnetically induced currents on electrified railway signaling systems in the United Kingdom. *Space Weather*, *21*(3), e2022SW003385. https://doi.org/10.1029/2022SW003385

Pérez-Alanis, C. A., Janvier, M., Nieves-Chinchilla, T., Aguilar-Rodríguez, E., Démoulin, P., & Corona-Romero, P. (2023). Statistical analysis of interplanetary shocks from Mercury to Jupiter. *Solar Physics*, *298*(60), 60. https://doi.org/10.1007/s11207-023-02152-3

Piccinelli, R., & Krausmann, E. (2018). North Europe power transmission system vulnerability during extreme space weather. *Journal of Space Weather and Space Climate*, *8*(A03), A03. https://doi.org/10.1051/swsc/2017033

Piersanti, M., & Carter, B. (2020). Geomagnetically induced currents. In M. Materassi, B. Forte, A. J. Coster, & S. Skone (Eds.), *The dynamical ionosphere: A systems approach to ionospheric irregularity* (pp. 121–134). Elsevier. https://doi.org/10.1016/B978-0-12-814782-5.00010-8

Pilipenko, V. A., Fedorov, E. N., Xu, Z., Hartinger, M. D., Engebretson, M. J., & Edwards, T. R. (2020). Incidence of alfvenic SC pulse onto the conjugate ionospheres. *Journal of Geophysical Research: Space Physics*, *125*(2), e2019JA027397. https://doi.org/10.1029/2019JA027397

Priest, E. F. (1981). *Solar magnetohydrodynamics*. D. Reidel Publishing.

Pulkkinen, A., Rastatter, L., Kuznetsova, M., Singer, H., Balch, C., Weimer, D., et al. (2013). Community-wide validation of geospace model ground magnetic field perturbation predictions to support model transition to operations. *Space Weather*, *11*(6), 369–385. https://doi.org/10.1002/swe.20056

Reeves, G. D., & Henderson, M. G. (2001). The storm-substorm relationship: Ion injections in geosynchronous measurements and composite energetic neutral atom images. *Journal of Geophysical Research*, *106*(A4), 5833–5844. https://doi.org/10.1029/2000JA003017

Rubtsov, A. V., Nos,́ M., Matsuoka, A., Shinohara, I., & Miyoshi, Y. (2023). Polarization and spatial distribution features of Pc4 and Pc5 waves in the magnetosphere. *Journal of Geophysical Research: Space Physics*, *128*(10), e2023JA031674. https://doi.org/10.1029/2023JA031674

Rudd, J. T., Oliveira, D. M., Bhaskar, A., & Halford, A. J. (2019). How do interplanetary shock impact angles control the size of the geoeffective magnetosphere? *Advances in Space Research*, *63*(1), 317–326. https://doi.org/10.1016/j.asr.2018.09.013

Russell, C. T., Chi, P. J., Dearborn, D. J., Ge, Y. S., Kuo-Tiong, B., Means, J. D., et al. (2008). THEMIS ground-based magnetometers. *Space Science Reviews*, *141*(1–4), 389–412. https://doi.org/10.1007/s11214-008-9337-0

Russell, C. T., Ginskey, M., & Petrinec, S. M. (1994). Sudden impulses at low-latitude stations: Steady state response for northward interplanetary magnetic field. *Journal of Geophysical Research*, *99*(A1), 253–261. https://doi.org/10.1029/93JA02288

Samsonov, A. A., Sergeev, V. A., Kuznetsova, M. M., & Sibeck, D. G. (2015). Asymmetric magnetospheric compressions and expansions in response to impact of inclined interplanetary shock. *Geophysical Research Letters*, *42*(12), 4716–4722. https://doi.org/10.1002/2015GL064294

Schwartz, S. J. (1998). Shock and discontinuity normals, Mach numbers, and related parameters. In G. Paschmann & P. W. Daly (Eds.), *Analysis methods for multi-spacecraft data* (pp. 249–270). ESA Publications Division.

Selvakumaran, R., Veenadhari, B., Ebihara, Y., Kumar, S., & Prasad, D. S. V. V. D. (2017). The role of interplanetary shock orientation on SC/SI rise time and geoeffectiveness. *Advances in Space Research*, *59*(5), 1425–1434. https://doi.org/10.1016/j.asr.2016.12.010

Shepherd, S. G. (2014). Altitude-adjusted corrected geomagnetic coordinates: Definition and functional approximations. *Journal of Geophysical Research: Space Physics*, *119*(9), 7501–7521. https://doi.org/10.1002/2014JA020264

Shi, Y., Oliveira, D. M., Knipp, D. J., Zesta, E., Matsuo, T., & Anderson, B. (2019). Effects of nearly frontal and highly inclined interplanetary shocks on high-latitude field-aligned currents (FACs). *Space Weather*, *17*(12), 1659–1673. https://doi.org/10.1029/2019SW002367

Sitnov, M., Birn, J., Ferdousi, B., Gordeev, E., Khotyaintsev, Y., Merkin, V., et al. (2019). Explosive magnetotail activity. *Space Science Reviews*, *215*(31), 31. https://doi.org/10.1007/s11214-019-0599-5

Smith, A. W., Rae, J., Forsyth, C., Oliveira, D. M., Freeman, P. M., & Jackson, D. (2020). Probabilistic forecasts of storm sudden commencements from interplanetary shocks using machine learning. *Space Weather*, *18*(11), e2020SW002603. https://doi.org/10.1029/2020SW002603

Smith, A. W., Rodger, C. J., Mac Manus, D. H., Forsyth, C., Rae, I. J., Freeman, M. P., et al. (2022). The correspondence between sudden commencements and geomagnetically induced currents: Insights from New Zealand. *Space Weather*, *20*(8), e2021SW002983. https://doi.org/10.1029/2021SW002983

Snyder, J. P. (1993). *Flattening the Earth: Two thousand years of map projections*. The University of Chicago Press.

Stepanov, N. A., Sergeev, V. A., Shukhtina, M. A., Ogawa, Y., Chu, X., & Rogov, D. D. (2021). Ionospheric electron density and conductance changes in the auroral zone during substorms. *Journal of Geophysical Research: Space Physics*, *126*(7), e2021JA029572. https://doi.org/10.1029/2021JA029572

Stone, R. G. & Tsurutani, B. T. (Eds.) (1985). Collisionless shocks in the heliosphere: A tutorial review, *Geophysical monograph series* (Vol. 34). American Geophysical Union. https://doi.org/10.1029/GM034

Su, Z.-P., Xiong, M., Zheng, H.-N., & Wang, S. (2009). Propagation of interplanetary shock and its consequent geoeffectiveness. *Chinese Journal of Geophysics*, *52*(2), 292–300. https://doi.org/10.1002/cjg2.1351

Takahashi, K., Elsden, T., Wright, A. N., & Degeling, A. W. (2023). Polarization of magnetospheric ULF waves excited by an interplanetary shock on 27 February 2014. *Journal of Geophysical Research: Space Physics*, *128*(9), e2023JA031608. https://doi.org/10.1029/2023JA031608

Takeuchi, T., Russell, C. T., & Araki, T. (2002). Effect of the orientation of interplanetary shock on the geomagnetic sudden commencement. *Journal of Geophysical Research*, *107*(A12), SMP6-1–SMP6-10. https://doi.org/10.1029/2002JA009597

Thaduri, A., Galar, D., & Kumar, U. (2020). Space weather climate impacts on railway infrastructure. *International Journal of System Assurance Engineering and Management*, *11*(Suppl 2), 267–281. https://doi.org/10.1007/s13198-020-01003-9

Tsurutani, B. T., & Hajra, R. (2021). The interplanetary and magnetospheric causes of geomagnetically induced currents (GICs) > 10 A in the Mäntsälä Finland pipeline: 1999 through 2019. *Journal of Space Weather and Space Climate*, *11*(23), 1–23. https://doi.org/10.1051/swsc/2021001

Tsurutani, B. T., & Lin, R. P. (1985). Acceleration of > 47 keV ions and > 2 keV electrons by interplanetary shocks at 1 AU. *Journal of Geophysical Research*, *90*(A1), 1–11. https://doi.org/10.1029/JA090iA01p00001

Viljanen, A., Tanskanen, E. I., & Pulkkinen, A. (2006). Relation between substorm characteristics and rapid temporal variations of the ground magnetic field. *Annales Geophysicae*, *24*(2), 725–733. https://doi.org/10.5194/angeo-24-725-2006

Villante, U., & Piersanti, M. (2011). Sudden impulses at geosynchronous orbit and at ground. *Journal of Atmospheric and Solar-Terrestrial Physics*, *73*(1), 61–76. https://doi.org/10.1016/j.jastp.2010.01.008

Wang, C., Li, C. X., Huang, Z. H., & Richardson, J. D. (2006). Effect of interplanetary shock strengths and orientations on storm sudden commencement rise times. *Geophysical Research Letters*, *33*(14), 1–3. https://doi.org/10.1029/2006GL025966

Wang, C., Li, H., Richardson, J. D., & Kan, J. R. (2010). Interplanetary shock characteristics and associated geosynchronous magnetic field variations estimated from sudden impulses observed on the ground. *Journal of Geophysical Research*, *115*(A9), A09215. https://doi.org/10.1029/2009JA014833

Wang, C.-R., Zong, Q.-G., & Wang, Y.-F. (2010). Propagation of interplanetary shock excited ultra low frequency (ULF) waves in magnetosphere-ionosphere-atmosphere—Multi-spacecraft "cluster" and ground-based magnetometer observations. *Science China Technological Sciences*, *53*(9), 2528–2534. https://doi.org/10.1007/s11431-010-4064-7

Wang, X., Liu, C., & Kang, Z. (2021). Effect of the Earth's lateral conductivity variations on geomagnetically induced currents in power grids. *International Journal of Electrical Power & Energy Systems*, *132*, 107148. https://doi.org/10.1016/j.ijepes.2021.107148

Waters, C. L., Anderson, B. J., Green, D. L., Korth, H., Barnes, R. J., & Vanhamäki, H. (2020). Science data products for AMPERE. In M. W. Dunlop & H. Lühr (Eds.), *Ionospheric multi-spacecraft analysis tools: Approaches for deriving ionospheric parameters* (Vol. 17, pp. 141–165). Springer International Publishing. https://doi.org/10.1007/978-3-030-26732-2_7

Welling, D. T., Love, J. J., Joshua Rigler, E., Oliveira, D. M., Komar, C. M., & Morley, S. K. (2021). Numerical simulations of the geospace response to a perfect interplanetary coronal mass ejection. *Space Weather*, *19*(2), e2020SW002489. https://doi.org/10.1029/2020SW002489

Weygand, J. M. (2021). The temporal and spatial development of *dB/dt* for substorms. *AIMS Geosciences*, *7*(1), 74–94. https://doi.org/10.3934/geosci.2021004

Weygand, J. M., Amm, O., Angelopoulos, V., Milan, S. E., Grocott, A., Gleisner, H., & Stolle, C. (2012). Comparison between superdarn flow vectors and equivalent ionospheric currents from ground magnetometer arrays. *Journal of Geophysical Research*, *117*(A5), A05325. https://doi.org/10.1029/2011JA017407

Weygand, J. M., Amm, O., Viljanen, A., Angelopoulos, V., Murr, D., Engebretson, M. J., et al. (2011). Application and validation of the spherical elementary currents systems technique for deriving ionospheric equivalent currents with the North American and Greenland ground magnetometer arrays. *Journal of Geophysical Research*, *116*(A3), A03305. https://doi.org/10.1029/2010JA016177

Weygand, J. M., Zesta, E., Kadokura, A., & Oliveira, D. M. (2022). Investigation of the differences in onset times for hemispherically conjugate magnetometers. *Frontiers in Astronomy and Space Science*, *9*(896199). https://doi.org/10.3389/fspas.2022.896199

Wing, S., Johnson, J. R., Chaston, C. C., Echim, M., Escoubet, C. P., Lavraud, B., et al. (2014). Review of solar wind entry into and transport within the plasma sheet. *Space Science Reviews*, *184*(1–4), 33–86. https://doi.org/10.1007/s11214-014-0108-9U2014

Winslow, R. M., Lugaz, N., Philpott, L. C., Schwadron, N. A., Farrugia, C. J., Anderson, B. J., & Smith, C. W. (2015). Interplanetary coronal mass ejections from MESSENGER orbital observations at Mercury. *Journal of Geophysical Research: Space Physics*, *120*(8), 6101–6118. https://doi.org/10.1002/2015JA021200

Xu, Z., Hartinger, M. D., Oliveira, D. M., Coyle, S., Clauer, C. R., Weimer, D., & Edwards, T. (2020). Inter-hemispheric asymmetries in the ground magnetic response to interplanetary shocks: The role of shock impact angle. *Space Weather*, *18*(3), e2019SW002427. https://doi.org/10.1029/2019SW002427

Zhou, X., & Tsurutani, B. T. (2001). Interplanetary shock triggering of nightside geomagnetic activity: Substorms, pseudobreakups, and quiescent events. *Journal of Geophysical Research*, *106*(A9), 18957–18967. https://doi.org/10.1029/2000JA003028

Zong, Q.-G., Zhou, X.-Z., Wang, Y. F., Li, X., Song, P., Baker, D. N., et al. (2009). Energetic electron response to ULF waves induced by interplanetary shocks in the outer radiation belt. *Journal of Geophysical Research*, *114*(A10204), 1–13. https://doi.org/10.1029/2009JA014393